The DOI for this manuscript is doi: 10.1175/BAMS-D-14-00255.1

Wendisch, M., U. Poschl, M. Andreae, L. Machado, R. Albrecht, H. Schlager, D. Rosenfeld, S. Martin, A. Abdelmonem, A. Afchine, A. Araujo, P. Artaxo, H. Aufmhoff, H. Barbosa, S. Borrmann, R. Braga, B. Buchholz, M. Cecchini, A. Costa, J. Curtius, M. Dollner, M. Dorf, V. Dreiling, V. Ebert, A. Ehrlich, F. Ewald,

G. Fisch, A. Fix, F. Frank, D. Fuetterer, C. Heckl, F. Heidelberg, T. Hueneke, E. Jaekel, E. Jaervinen, T. Jurkat, S. Kanter, U. Kaestner, M. Kenntner, J. Kesselmeier, T. Klimach, M. Knecht, R. Kohl, T. Koelling, M. Kraemer, M. Krueger, T. Krisna, J. Lavric, K. Longo, C. Mahnke, A. Manzi, B. Mayer, S. Mertes, A. Minikin, S. Molleker, S. Muench, B. Nillius, K. Pfeilsticker, C. Poehlker, A. Roiger, D. Rose, D. Rosenow, D. Sauer, M. Schnaiter, J. Schneider, C. Schulz, R. de Souza, A. Spanu, P. Stock, D. Vila, C. Voigt, A. Walser, D. Walter, R. Weigel, B. Weinzierl, F. Werner, M. Yamasoe, H. Ziereis, T. Zinner, and M. Zoeger, 2016: The ACRIDICON-CHUVA campaign: Studying tropical deep convective clouds and precipitation over Amazonia using the new German research aircraft HALO. Bull. Amer. Meteor. Soc. doi:10.1175/BAMS-D-14-00255.1, in press.

The ACRIDICON–CHUVA campaign: Studying tropical deep convective clouds and precipitation over Amazonia using the new German research aircraft HALO

Revised manuscript for submission to *Bull. Am. Meteorol. Soc.*, **January 14, 2016**

Manfred Wendisch (0,1), Ulrich Pöschl (2), Meinrat O. Andreae (3), Luiz A. T. Machado (4), Rachel Albrecht (5), Hans Schlager (6), Daniel Rosenfeld (7), Scot T. Martin (20), Ahmed Abdelmonem (14), Armin Afchine (13), Alessandro Araùjo (23), Paulo Artaxo (25), Heinfried Aufmhoff (6), Henrique M. J. Barbosa (25), Stephan Borrmann (16,17), Ramon Braga (4), Bernhard Buchholz (8), Micael Amore Cecchini (4), Anja Costa (13), Joachim Curtius (9), Maximilian Dollner (18,6), Marcel Dorf (2), Volker Dreiling (21), Volker Ebert (8), André Ehrlich (1), Florian Ewald (18), Gilberto Fisch (10), Andreas Fix (6), Fabian Frank (9), Daniel Fütterer (6), Christopher Heckl (6), Fabian Heidelberg (6), Tilman Hüneke (11), Evelyn Jäkel (1), Emma Järvinen (14), Tina Jurkat (6), Sandra Kanter (1), Udo Kästner (15), Mareike Kenntner (6), Jürgen Kesselmeier (3), Thomas Klimach (2), Matthias Knecht (11), Rebecca Kohl (9), Tobias Kölling (18), Martina Krämer (13), Mira Krüger (2), Trismono Candra Krisna (1), Jost V. Lavric (24), Karla Longo (4), Christoph Mahnke (17), Antonio O. Manzi (22), Bernhard Mayer (18), Stephan Mertes (15), Andreas Minikin (21), Sergej Molleker (17), Steffen Münch (9), Björn Nillius (2), Klaus Pfeilsticker (11), Christopher Pöhlker (3), Anke Roiger (6), Diana Rose (9), Dagmar Rosenow (1), Daniel Sauer (18,6), Martin Schnaiter (14), Johannes Schneider (16), Christiane Schulz (16), Rodrigo A. F. de Souza (19), Antonio Spanu (6), Paul Stock (6), Daniel Vila (4), Christiane Voigt (6,17), Adrian Walser (18,6), David Walter (3), Ralf Weigel (17), Bernadett Weinzierl (18,6), Frank Werner (1,12), Marcia A. Yamasoe (5), Helmut Ziereis (6), Tobias Zinner (18), Martin Zöger (21)

(0) Corresponding author, e-mail: m.wendisch@uni-leipzig.de

(1) Leipziger Institut für Meteorologie (LIM), Universität Leipzig, Stephanstr. 3, 04103 Leipzig, Deutschland

(2) Multiphase Chemistry Department, Max Planck Institute for Chemistry (MPIC), Mainz, Deutschland

(3) Biogeochemistry Department, Max Planck Institute for Chemistry (MPIC), Mainz, Deutschland

(4) Instituto Nacional de Pesquisas Espaciais (INPE), Centro de Previsão de Tempo e Estudos Climáticos, São José dos Campos, Brasil

(5) Departamento de Ciências Atmosféricas, Instituto de Astronomia, Geofísica e Ciências Atmosféricas, Universidade de São Paulo, Brasil

(6) Institut für Physik der Atmosphäre, Deutsches Zentrum für Luft– und Raumfahrt (DLR), Oberpfaffenhofen, Deutschland

(7) Program of Atmospheric Sciences, Institute of Earth Sciences, The Hebrew University of Jerusalem, Israel

(8) Physikalisch–Technische Bundesanstalt (PTB), Braunschweig, Deutschland

(9) Institut für Atmosphäre und Umwelt (IAU), Universität Frankfurt, Deutschland

(10) Departamento de Ciência e Tecnologia Aeroespacial, Instituto de Aeronaútica e Espaço, São José dos Campos, Brasil

(11) Institut für Umweltphysik (IUP), Universität Heidelberg, Deutschland

(12) Now at University of Maryland, Baltimore County, USA

(13) Forschungszentrum Jülich (FZJ), Deutschland

(14) Karlsruhe Institute of Technology (KIT), Institute of Meteorology and Climate Research,

Karlsruhe, Deutschland

(15) Leibniz–Institut für Troposphärenforschung (TROPOS), Leipzig, Deutschland

(16) Particle Chemistry Department, Max Planck Institute for Chemistry (MPIC), Mainz, Deutschland

(17) Institut für Physik der Atmosphäre (IPA), Johannes Gutenberg-Universität, Mainz, Deutschland

(18) Meteorologisches Institut, Ludwig–Maximilians–Universität (LMU), München, Deutschland

(19) Departamento de Meteorologia, Universidade do Estado do Amazonas, Manaus, Amazonas, Brasil

(20) School of Engineering and Applied Sciences, Harvard University, Cambridge, MA, USA

(21) Flugexperimente, Deutsches Zentrum für Luft- und Raumfahrt (DLR), Oberpfaffenhofen, Deutschland

(22) Instituto Nacional de Pesquisas Espaciais da Amazônia (INPA), Clima e Ambiente (CLIAMB), Manaus, Brasil

(23) Empresa Brasileira de Pesquisa Agropecuária (EMBRAPA), Belém, Brasil

(24) Max Planck Institute for Biogeochemistry, Jena, Deutschland

(25) Instituto de Física, Universidade de São Paulo, Brasil

Capsule summary: Comprehensive in–situ and remote sensing observations of deep convective clouds from below base to anvils using the new German research jet aircraft HALO (High Altitude and LOng Range research aircraft) have been performed over Amazonia to study the influence of anthropogenic aerosols on the cloud life cycle and precipitation formation processes.

Abstract: Between 1 September and 4 October 2014 a combined airborne and ground–based measurement campaign was conducted to study tropical deep convective clouds over the Brazilian Amazon rainforest. The new German research aircraft HALO, a modified Gulfstream G550, and extensive ground–based instrumentation were deployed in and near Manaus (State of Amazonas). The campaign was part of the German–Brazilian ACRIDICON–CHUVA venture to quantify aerosol–cloud–precipitation interactions and their thermodynamic, dynamic, and radiative effects by in–situ and remote sensing measurements over Amazonia. The ACRIDICON–CHUVA field observations were carried out in cooperation with the second Intensive Operating Period of GoAmazon2014/5. In this paper we focus on the airborne data measured on HALO, which was equipped with about 30 in–situ and remote sensing instruments for meteorological, trace gas, aerosol, cloud, precipitation, and spectral solar radiation measurements. Fourteen research flights with a total duration of 96 flight hours were performed. Five scientific topics were pursued: (a) cloud vertical evolution and life cycle (cloud profiling), (b) cloud processing of aerosol particles and trace gases (inflow and outflow), (c) satellite and radar validation (cloud products), (d) vertical transport and mixing (tracer experiment), and (e) cloud formation over forested/deforested areas. Data were collected in near–pristine atmospheric conditions and in environments polluted by biomass burning and urban emissions. The paper presents a general introduction of the ACRIDICON–CHUVA campaign (motivation and addressed research topics) and of HALO with its extensive instrument package, as well as a presentation of a few selected measurement results acquired during the flights for some selected scientific topics.

1. Introduction

Tropical deep convective clouds profoundly influence the atmospheric energy budget and hydrological cycles and often cause severe weather events (gusts, hail, squall lines, lightning, thunderstorms, flooding). They transfer major parts of the surface solar heating to the atmosphere by releasing latent heat during thermodynamic phase transitions (condensation, freezing); on the other hand deep convective clouds consume heat energy by melting and evaporation. These energy transfers are realized along various thermodynamic pathways, depending on the availability and the properties of Cloud Condensation Nuclei (CCN) and Ice Nuclei (IN) (Rosenfeld et al. 2008; Tao et al. 2012), and on thermodynamic conditions (atmospheric gases), which impact the vertical development, microphysical properties, cloud top height, and electrification of deep convective clouds (Wang and Prinn 2000; Williams et al. 2002; Kolb et al. 2010; Li et al. 2011; Albrecht et al. 2011; Morrison and Grabowski 2013; Fan et al. 2013).

To understand the life cycle of deep convective clouds, their temporal evolution from the cloud base through the mixed–phase level all the way up to the anvil needs to be observed (Rosenfeld et al. 2008; Heintzenberg and Charlson 2009; Rosenfeld et al. 2014). In addition, the complex interactions between cloud, precipitation, aerosol particles, and trace gases depend on dynamic conditions such as the vertical wind shear (Khain et al. 2009, 2008; Fan et al. 2009; Albrecht et al. 2011; Fan et al. 2012; Lebo and Morrison 2014).

The realistic description of precipitation formation in tropical deep convective clouds and the consequences for the hydrological cycle still entail many open issues (Rosenfeld 1999; Machado et al. 2014). In this regard, the impact of changes in land use (deforestation of pristine tropical forest turned into pasture sites mainly for agricultural purposes) is debated, which is a major issue in particular in the tropical rainforests of Amazonia (Durieux et al. 2003; Negri et al. 2004; Fisch

et al. 2004; Wang et al. 2010; Albrecht et al. 2011). For example, it is known that the sensible heat flux is higher over pasture than forest (Shukla et al. 1990). Furthermore, Cutrim et al. (1995) showed an increase in cloud cover over deforested areas, and Neves and Fisch (2015) have detected that the deforested areas exhibit a deeper boundary layer than pristine tropical forest regions.

To study these open problems related to tropical deep convective clouds the combined ACRIDICON–CHUVA campaign was performed. ACRIDICON stands for "Aerosol, Cloud, Precipitation, and Radiation Interactions and Dynamics of Convective Cloud Systems"; CHUVA is the acronym for "Cloud processes of tHe main precipitation systems in Brazil: A contribUtion to cloud resolVing modeling and to the GPM (Global Precipitation Measurements)". A major objective was to quantify the influence of aerosol particles and trace gases (natural and anthropogenic) on cloud evolution and precipitation formation. Furthermore, the cloud thermodynamic, dynamic, and radiative effects were investigated. This involved observations of (a) the clouds' life cycle (including the vertical evolution of cloud properties), (b) the cloud processing of aerosol particles and trace gases (inflow at cloud base and outflow at greater heights out of the anvil), (c) the validity of satellite and radar cloud products, (d) the vertical transport and mixing of trace gases and aerosol particles by deep convective clouds, and (e) the effects of deforestation and biomass burning on cloud evolution.

The ACRIDICON–CHUVA field observations took place in Amazonia. The campaign was centered on the environment of Manaus, a city of two million people. Manaus is an isolated urban area in the central Amazon Basin situated at the confluence of the two major tributaries of the Amazon river. Outside this industrial city there is mostly natural forest for over 1000 to 2000 km in every direction. This makes it possible to study the impact of local pollution on cloud evolution by taking measurements upwind and downwind of the city. ACRIDICON–CHUVA was intentionally planned to take place at a time of year (September–October) when the non–

linear interactions between modified cloud microphysics (by higher concentrations of CCN) and thermodynamics (by land cover contrasts) were amplified. It is during the transition between dry to wet season (September–October) that the gradual large–scale advection of humidity in the troposphere increases the conditional thermodynamical instability, while biomass burning peaks just before first rainfalls. This allows the separation of the individual effects on deep convection.

The German HALO (High Altitude and LOng Range research aircraft) and a suite of ground–based instruments were deployed during ACRIDICON–CHUVA. HALO (see http://www.halo.dlr.de/) is an Ultra Long Range Business Jet G 550 (manufactured by Gulfstream); it is of similar type as the United States High–Performance Instrumented Airborne Platform for Environmental Research (HIAPER) (Laursen et al. 2006). HALO with its high ceiling altitude (up to 15 km) and long endurance (up to eight hours) is capable of collecting airborne in–situ and remote sensing measurements of cloud microphysical and radiative properties, aerosol characteristics, and chemical tracer compounds in and around tropical deep convective clouds, which are needed to study the open scientific issues discussed above. Serious difficulties in obtaining such measurements during previous campaigns include icing of aircraft during cloud penetrations, limited ceiling to reach the top of deep convective clouds, and insufficient endurance to study the cloud life cycle, among others. HALO provides unique opportunities to overcome these issues, although aircraft icing still remains a problem.

The ACRIDICON–CHUVA campaign was performed in cooperation with the second Intensive Operating Period (IOP2) of the Observations and Modeling of the Green Ocean Amazon (GoAmazon2014/5) experiment (Martin et al. 2015), which collected data over a two–years period (2014–2015). The GoAmazon2014/5 campaign sought to quantify and understand how aerosol and cloud life cycles in a particularly background (relatively clean) in the tropics are influenced by pollutant outflow from a large tropical city. The project addressed the susceptibility of cloud–

aerosol–precipitation interactions to present–day and future pollution in the tropics. As part of GoAmazon2014/5, there were six ground stations in and around Manaus as well as coordinated flights of HALO with a Gulfstream–1 (G1) aircraft. The G1, compared to HALO, flew more slowly and at lower altitudes. Coordinated flights of the HALO and G1 aircraft took place during IOP2 to provide simultaneous in–situ measurements at different altitudes in and around Manaus. In one set of flights, the two aircraft operated in formation so that they could intercompare and cross–calibrate instrumentation. In another set of flights, the G1 flew at lower altitudes while HALO flew at higher altitudes so that a simultaneous profile of cloud–related properties below, in, and above clouds was measured. Neither aircraft operating alone could have achieved these observations.

Only few previous aircraft missions had been specifically devoted to deep convective clouds in Amazonia. The first important effort was made during the Tropical Rainfall Measuring Mission (TRMM)–Large Scale Biosphere Atmosphere Experiment in Amazonia (LBA) campaign. It focused on the dynamical, microphysical, electrical, and diabatic heating characteristics of tropical convection in the Amazon region. The NASA ER–2 and the Citation II from the University of North Dakota collected cloud data in January–February 1999. The main goal was to validate TRMM observations and retrievals; no special attention was paid to the contrast between polluted and pristine cloud conditions. Results have been published by e.g., Heymsfield et al. (2002); Stith et al. (2002); Anderson et al. (2005). Basically the results from the TRMM–LBA campaign presented the first description of cloud microphysical properties in Amazonia during the wet season. The LBA–SMOCC (LBA–Smoke, Aerosols, Clouds, Rainfall, and Climate) campaign was held in the Amazon region from September to November in 2002. Two Brazilian airplanes were used, from Instituto Nacional de Pesquisas Espaciais (INPE) and Ceará Federal University, both limited to 4 km ceiling altitude. The aircraft from INPE carried aerosol measuring instruments;

the second aircraft was equipped with cloud microphysical probes. From the data obtained, Andreae et al. (2004) classified precipitation regimes as function of aerosol loading. They concluded that smoke from forest fires reduced cloud droplet size and delayed the onset of precipitation. The aerosol/cloud/precipitation component of ACRIDICON–CHUVA was conceived as a direct follow–on to the LBA–SMOCC campaign, which had been limited in altitude, range, and instrumentation. In 2004 the TROCCINOX (Tropical convection and its impact on the troposphere and lower stratosphere) campaign was carried out over the tropical area around Bauru. It focused on influences of convective clouds on the transformation and transport of chemical trace gas species, on new particle formation, and on lightning (see special issue on TROCCINOX in *Atmos. Chem. Phys.* at http://www.atmos–chem–phys.net/special_issue82.html). Previous campaigns with emphasis on aerosol particle properties in the Amazon region were reviewed by Martin et al. (2010). In 2014, the South AMerican Biomass Burning Analysis (SAMBBA) campaign took place in Amazonia. Its main goal was to evaluate the chemical properties of fire emissions in Amazonia.

The focus in the present paper is to introduce the specific processes of deep convective clouds in Amazonia (Section 2), to elaborate the research topics addressed by the ACRIDICON–CHUVA campaign (Section 3), to introduce HALO and its instrumentation (Section 4a), to provide an overview of the conducted research flights (Section 4b), to characterize the general meteorological and pollution conditions during the campaign (Section 4c), and finally to show exemplary results of the observations analyzed so far (Section 5). The paper is meant as a reference for a series of future detailed scientific publications resulting from the ACRIDICON–CHUVA campaign.

2. Specifics in Amazonia

a. Deep convective clouds during the dry season

To illustrate the processes taking place in tropical deep convective clouds in Amazonia during the dry season (May to August), Fig. 1 shows a conceptual diagram of the effects of increased CCN and IN concentrations. Convective updraft is primarily controlled by the latent and sensible heat of the surface and atmosphere (Silva Dias et al. 2002; Williams et al. 2002). During the transition from the dry to wet season (September to October), sensible heating over deforested areas is increased, increasing cloud base heights and creating conditional instability. The enhanced cloud base updrafts also increase cloud base supersaturation and cloud droplet concentrations (Reutter et al. 2009; Chang et al. 2015; Zheng and Rosenfeld 2015). In the same season, biomass burning increases CCN concentrations and consequently the number of nucleated cloud droplets with reduced sizes (Rosenfeld and Lensky 1998; Andreae et al. 2004). The smaller cloud droplet size slows the collision–coalescence and moves the rain initiation to greater (cooler) heights, leading to more Supercooled Liquid Water (SLW) in the mixed–phase region. This enhances the production of ice hydrometeors in higher (colder) altitudes, increases latent heating to higher levels, strengthens updraft and enhances electrification and lightning (Rosenfeld et al. 2008). More ice in greater altitudes of the clouds will also extend the anvils and moisten the upper troposphere. Indeed, Durieux et al. (2003) demonstrated that during the wet season convective clouds have higher cloud tops over deforested regions, and during the dry season deforested areas have more low level clouds than forested regions. Also, Gonçalves et al. (2014) show large precipitation in Manaus, during the dry to wet season, when the environment is more polluted and the atmosphere is unstable.

Ice nuclei concentrations are at least five orders of magnitude smaller than CCN concentrations. At the lower bounds of supersaturation, S, that particles typically encounter during the cloud formation process [about 0.1–0.2 %, Krüger et al. (2014)], CCN concentrations are usually in the range between 100 and 1000 cm^{-3} (Paramonov et al. 2015). The CCN concentrations depend strongly on the total aerosol particle number concentration and make up about 10 % of the sub–micrometer particles at $S = 0.1$ %. For higher supersaturations (e.g., $S = 1$ %) and large fractions of accumulation mode particles, the CCN fraction can easily amount to 60 % of the total particle concentration (Paramonov et al. 2015). In contrast, IN concentrations typically range between 1 and 10 per liter at a temperature of –20 °C and decrease with increasing temperature (DeMott et al. 2010). There is only one campaign in the Amazon region for which both CCN and IN measurements exist (AMAZE–08, Amazonian Aerosol Characterization Experiment); the CCN and IN concentrations were 41–90 cm^{-3} for $S = 0.1 - 0.2$ % (Gunthe et al. 2009) and 0.5–2 per liter for a temperature of –20 °C (DeMott et al. 2010), respectively.

In the dry season, a larger fraction of the precipitation will be produced in the mixed–phase region, by riming of supercooled cloud droplets onto ice particles and by migration of water vapor to liquid water and ice particles. Ice at temperatures warmer than –35 °C must be initiated by IN. Heterogeneous nucleation of ice particles usually occurs at temperatures below -12 °C by contact of IN with or immersion into supercooled drops. However, abundant ice is found occasionally in growing cloud elements at higher temperatures, coming from a process where very few IN can lead to a much larger number of ice particles. Therefore, an important challenge is to identify these rare particles that can serve as IN at temperatures as high as –5 °C (Hallett and Mossop 1974). These few newly formed ice particles will then collect supercooled cloud droplets and produce numerous ice splinters during the riming process, leading to a fast multiplication of ice particle concentrations, which increases precipitation. However, this ice multiplication is only effective

if the supercooled cloud droplets are sufficiently large to have a considerable collision efficiency with ice particles. Therefore, in extremely polluted environments, where cloud droplet sizes are decreased, the riming efficiency is drastically reduced as well as the ice multiplication, leading to larger amounts of supercooled cloud water and the production of larger ice hydrometeors and even hail (Andreae et al. 2004). Biological IN (e.g., bacteria, fungal spores) will raise freezing temperatures as they will freeze water at temperatures warmer than $-5\,^{\circ}\mathrm{C}$ (Despres et al. 2012). Additionally, larger concentrations of IN can significantly increase ice particle number and mass in cloud anvils under tropical humid conditions. Depending on the location and season, the Amazon region offers ideal opportunities to study the contrast of cloud properties and aerosol–cloud interactions under near–pristine versus highly polluted conditions (Andreae et al. 2004; Pöschl et al. 2010).

b. Biomass burning

In central and southwest Amazonia, extensive areas of biomass burning are found during the dry (May to August) and dry–to–wet transition (September and October) seasons (Andreae et al. 2015). During these periods, logging, agriculture and livestock are primarily managed by setting fire to clean out recently deforested regions or to prepare the soil in old pasture areas for livestock and seasonal crops. These fire outbreaks release large amounts of aerosol particles and CCN into the atmosphere (Artaxo et al. 2002; Roberts et al. 2003), while large patches of deforestation and pasture change the partitioning of latent and sensible heating at the surface. In particular, black carbon particles are emitted, which may influence precipitation formation (Gonçalves et al. 2014). The surface heating contrast between deforested and forested areas is enhanced during the dry season due to the low rainfall amounts. In consequence, more intense turbulent transients within the planetary boundary layer are generated leading to higher cloud base heights (Fisch et al. 2004),

modified thermodynamic profiles (Albrecht et al. 2011), and induced local circulations (Silva Dias et al. 2002; Baidya Roy 2009). All these processes impact cloud cover and rainfall (Negri et al. 2004; Chagnon and Bras 2005; Baidya Roy 2009; Wang et al. 2010). Large concentrations of CCN increase the number and reduce the size of cloud droplets, which is called the Twomey or first indirect aerosol effect (Rosenfeld and Lensky 1998; Andreae et al. 2004).

3. Research topics and resulting flight patterns

In the framework of the general objectives of ACRIDICON–CHUVA, as outlined in Section 1, five major research topics (realized by specific flight patterns) were pursued, which are briefly introduced in this section.

a. Cloud vertical evolution and life cycle (cloud profiling)

The vertical evolution (from cloud base to anvil) of deep convective clouds was mapped during different stages of the clouds' life cycle. Also, the initiation and development of precipitation particles in growing convective clouds was tracked. For this purpose the:

- microphysical, i.e., droplet/ice particle number concentration, Droplet Size Distribution (DSD), Liquid Water Content (LWC), Ice Water Content (IWC), droplet effective radius, thermodynamic phase, structure/shape, composition, mixing state, cloud condensation and ice nucleation activity,
- macrophysical (cloud horizontal cover and vertical extent), and
- dynamic (updraft velocities, turbulence)

properties of tropical deep convective cloud systems as a function of height above cloud base were measured under different levels of air pollution (i.e., trace gases and aerosol particles).

The corresponding schematic flight pattern to realize the vertical mapping is sketched in Fig. 2a. It started by probing the aerosol particle and trace gas distributions as well as the dynamic properties below cloud base (white arrows), then crossing the clouds at different altitudes (as icing allowed) and sampling the lower cloud parts (green arrows), ascending through the young developing cloud elements in the upshear growing stages (dashed red line), all the way to the level of the anvil. In cloud–free parts of this section of the flight pattern spectral solar radiation reflected by cloud sides was measured to obtain vertical information about the cloud microphysical properties. Then, the cloud anvil and the outflow region (exhaust of the cloud) were sampled to look at cloud–processed aerosol particles and trace gases (blue arrow). Finally, HALO flew above clouds in order to perform passive airborne remote–sensing measurements from above the cloud (yellow arrow) using downward–looking solar spectral radiometers and imaging spectrometers (see Section 4). These over–flights were conducted along the wind shear. Such cloud profile data were taken at locations with similar thermodynamic conditions but contrasting aerosol content.

b. Cloud processing of aerosol particles and trace gases (inflow and outflow)

The physical and chemical properties of trace gases, aerosol and cloud particles in the inflow, in the interior, and in the outflow of deep convective clouds were measured, as well as their changes in the course of cloud evolution. For this purpose, the vertical redistribution of aerosol particles and trace gases by convective systems, the particle formation processes and the evolution of aerosol properties in the fresh and aged outflow of convective cloud cells were investigated. Particle Size Distribution (PSD), mixing state, and particle chemical properties were characterized in inflow and outflow regions. Also, the role of Black Carbon (BC) particles as CCN and their deposition by precipitation and ice crystals were investigated.

The schematic flight pattern designed to cover this research topic is illustrated in Fig. 2b. The trace gases and aerosol particles were characterized by in–situ and airborne remote sensing measurements, at first in the boundary layer (inflow) and then –after stepwise climbing to the anvil– in the outflow region (inside and outside the anvil). The long endurance and high ceiling of HALO allowed surveying the outflow at several altitudes and in several directions from the convective core. Also entrainment and detrainment in the altitude regions between inflow and outflow (by circling around the cell at different altitude levels) were measured.

c. Satellite and radar validation (cloud products)

The validation of satellite data using dedicated ground–based radar measurements in combination with airborne remote sensing and in–situ data is important to evaluate space–borne cloud products. These data provide a more continuous (compared to sporadic aircraft campaigns) and expanded (as compared to the local ground–based radar data) view on the properties and evolution of tropical deep convective cloud systems. The strategy to validate the cloud products from satellite measurements is to compare, in a first step, the quantities directly measured by satellite, ground–based radar, and airborne instrumentation (solar radiance, reflectivity). In a second step, satellite products such as cloud optical thickness, particle effective radius, liquid and ice water path, and thermodynamic phase derived by retrieval algorithms applied to ground–based radar, airborne and satellite observations have been validated. One question to be answered is whether the combination of the aircraft remote sensing instruments with the ground–based radar and satellite data can actually improve the quality of the derived microphysical profiles of cloud properties. Furthermore, the in–situ data measured by instruments mounted on the aircraft were compared with the data retrieved from the remote sensing measurements. Also, we investigated whether radiative transfer simulations based on the derived cloud profiles realistically represent the measured

solar and terrestrial radiation budget of deep convective cloud systems, and how important it is to consider the three-dimensional (3D) microphysical cloud structure in this regard.

For the validation of the satellite products, designated flights below and above clouds were carried out. Three flights were closely synchronized with overpasses of the A–Train set of satellite sensors, including MODIS (Moderate Resolution Imaging Spectroradiometer), CloudSat, CALIPSO (Cloud–Aerosol Lidar and Infrared Pathfinder Satellite Observations), and the GPM (Global Precipitation Measurements) satellite project. Additional legs through the cirrus outflow and for in–situ sampling followed. In order to combine and compare ground–based radar and airborne in–situ measurements, dedicated flight patterns above the radars were carried out. The flight patterns to cover this research topic were realized in combination with those introduced in Fig. 2.

d. Vertical transport and mixing (tracer experiment)

This research topic investigated how air masses were transported, entrained, and scavenged by tropical deep convective cloud systems. An artificial tracer (PFCs: Perfluorocarbons) was released below the cloud, and then sampled after it had spread. Additionally, a second tracer method was applied that used two atmospheric pollutants of common origin (e.g., emitted by biomass burning), but widely different atmospheric lifetimes, for example CO and HCHO (formaldehyde). Both approaches allow studying vertical air mass transport associated with deep convective clouds and entrainment to characterize the type and degree of pollution in the air masses where convection occurs, and to quantify the redistribution of air pollutants and their scavenging by tropical deep convective clouds.

After their release, the PFCs were probed by low–level horizontal flights measuring below the cloud after a certain amount of time had elapsed in order for the tracer to become homogeneously distributed. After one or two hours, the outflow was sampled. In the meantime, the entrainment

region of the cloud was investigated. For quantification of scavenging of trace species in the convective cloud, the concentration ratios of the trace gases and aerosol particles relative to the inert artificial (PFCs) and ambient (CO) tracers were measured in the inflow and outflow air. Therefore, the inflow air was characterized after release, dispersion, and mixing of the PFCs. These measurements were corroborated by measurements of chemical tracers of widely different atmospheric life–times (e.g., CO, HCHO) emitted from a common source (e.g., biomass burning). The change with time in the concentration ratio of the two tracers with a known emission ratio was used to determine the air mass age as function of height and location. The tracer experiments were combined with flights studying research topic b) (see flight pattern shown in Fig. 2b).

e. Cloud formation over forested/deforested areas

The measurements of atmospheric variables like wind, temperature, and water vapor as well as the microphysical and radiation parameters were used to evaluate the evolution of the atmospheric boundary layer, and the cloud microphysical and radiative processes that are important to investigate the differences in convective cloud formation over forested versus deforested areas. The question to be answered is whether the cloud microphysical properties and processes over tropical rainforest and deforested regions were significantly different.

The flights during the ACRIDICON–CHUVA campaign allowed a statistical description of the clouds forming over tropical rainforest and deforested regions in polluted (biomass burning) and background environments. During several flights, measurements over tropical rainforest and deforested regions were conducted. Three layers were measured: base, middle, and top of the cloud.

One flight (on 27 September 2014) was specifically devoted to this research topic. Two forested/deforested regions were selected and different strategies measuring at the same level over different vegetation types were applied to avoid aerosol and thermodynamical differences between

the measurements of the two vegetation types. The first flight track was over the Parque Nacional da Amazônia (4.2°S, 57.0°W); the flight was from West to East (see also Fig. 6), from the forest to the Transamazônica Road (BR–230) around Itaituba city. This flight path covered 65 km of forest and around 65 km of deforested region. The second flight path was over the Parque Nacional do Jamanxim (5.9°S, 55.3°W); the flight track was from North to South, from the National Park to the deforested region around the BR–163 road that links Brasília to Santarém and covered nearly the same path of 65 km over forest and deforested areas.

4. HALO instrumentation and flights, and general meteorological and pollution conditions

a. Instrumentation of HALO

The instruments installed on HALO during the ACRIDICON–CHUVA campaign are listed in Table 1. The details of the principle of operation of most of the listed devices are described in Wendisch and Brenguier (2013), additional references are given in Table 1. The cabin instruments were connected to respective inlets (gas sensors to a TGI, aerosol instruments to either HASI or the HALO–CVI, cloud residuum probes to the HALO–CVI), which were switched during the flight between HASI and HALO–CVI, depending on the specific purpose. Photos of the inlets and a sketch of the instrument locations in the cabin are presented in Figs. 3 and 4. Several instruments were installed in wing probes and inside the aircraft cabin to measure microphysical properties of aerosol particles, CCN and IN, droplets, ice crystals, and precipitation particles covering the size range from 5 nm (aerosol particles) to 6.4 mm (precipitation elements). Two instruments focused on the cloud active fraction of the aerosol population detecting aerosol particles that can be activated and grow to cloud droplets, and measuring the ice–active particles.

The cloud and precipitation probes were one of the backbones of the HALO instrumentation during the ACRIDICON–CHUVA campaign. They were installed beneath the wings of HALO (see Fig. 5). All cloud probe inlet entries and tips were modified to minimize the area susceptible to shattering of ice particles. Further, the probes were equipped with the 'particle–by–particle option', i.e., each particle was recorded individually including its own timestamp, which made a particle inter–arrival time analysis and a subsequent removal of most of the shattered ice crystal fragments possible. A comparison between the CAS using an inlet and the corresponding open–path CDP yielded good agreement, showing that shattering –which was especially feared to happen at the inlet of the CAS– was successfully minimized.

b. HALO flights

Fourteen scientific flights (labeled AC07 to AC20) with a total number of 96 flight hours were conducted in Brazil over Amazonia during the ACRIDICON–CHUVA campaign. More than 40 additional flight hours were spent for electromagnetic noise and instrument testing (AC01 to AC04) needed to obtain the campaign certification, and the ferry flights from Germany to Manaus (AC05, AC06) and back to Germany (AC21 and AC22). A summary of the flights performed in Brazil including information on the research topics pursued during each flight is given in Table 2. A narrative record of the campaign is available in blog form at http://acridicon-chuva.weebly.com

The long endurance of HALO allowed covering a wide geographic area and different pollution conditions within one flight (see the flight tracks illustrated in Fig. 6). The high ceiling altitude and the long endurance of HALO were utilized on most flights, which becomes obvious from the time series of flight altitudes presented in Fig. 7. Half of the flights took more than seven hours, and occasionally an altitude of 15 km was reached. On the other hand, the combination of long

endurance and high ceiling altitude made it possible to study the life cycle of individual convective clouds with high vertical resolution over a long time.

c. General meteorological and pollution conditions

The annual cycle of the sun produces a large–scale, low–level convergence movement from the central part (during austral summer) to the northwest part (spring) of South America and this controls the Amazonian convection and rainfall (Horel et al. 1989). The field campaign was conducted during the transition from the dry to the onset of the wet season, a period when local farmers and regional forestry industries set fire to pastures and freshly cut forest regions in order to prepare the land for the upcoming rainfalls.

In order to describe the general weather and pollution conditions during the ACRIDICON–CHUVA campaign, Fig. 8 shows time series of selected meteorological variables (air temperature, wind direction, precipitation), of the concentrations of pollution tracers such as CO and BC, as well as of several aerosol parameters (particle number concentration and size distribution) from measurements at the Amazon Tall Tower Observatory (ATTO) site, which is located 150 km NE of Manaus (Andreae et al. 2015). The data were taken at 60 m above ground. At the ATTO site, meteorological, trace gas and aerosol measurements are regularly conducted above the forest canopy within the framework of a long–term measurement program. Periods of individual flights are marked by vertical lines and labeled with flight numbers (see also Table 2). The general meteorological conditions during September 2014 were characterized by prevailing easterly wind directions, relatively high temperatures, and low rainfall with little day–to–day variability. Aerosol and CO time series show an oscillation of the atmospheric state between moderate and substantial anthropogenic pollution levels.

The vertical temperature profiles measured during all flights of the ACRIDICON–CHUVA campaign were rather similar (not shown). The stratosphere was not reached during the flights, since the cold point tropopause is usually located around 18 km in the tropics. In contrast, the relative humidity fields strongly depended on the actual water vapor situation.

5. Exemplary results

The detailed data analysis of the ACRIDICON–CHUVA campaign is ongoing and will be published. Below, some selected first results are discussed.

a. Cloud microphysical in–situ measurements in warm clouds

A set of DSDs was measured in warm convective clouds. Most clouds were penetrated by a visual selection of tops of growing convective elements. This assured that clouds were penetrated at the same phase of their life cycle, and that no precipitation fell from above into the measured cloud volume. Respective results of microphysical measurements are plotted as a function of altitude in Figs. 9–11.

Figure 9a presents the DSD data measured at different altitudes for a relatively clean (pristine, background) cloud case (AC09), whereas the DSDs plotted in Fig. 9b show measurements collected in polluted (biomass burning, smoky) convective clouds observed during AC12. In the clean clouds the droplets grow to large drops in the mm–size range and form rain, whereas for the polluted case the cloud droplets do not coalesce and form only negligible amounts of precipitation–size drops. The polluted clouds contain more small and fewer large droplets compared to the pristine clouds. These statements are confirmed by Fig. 10, which shows selected DSDs from the same flights, which are representative for the cloud top (Fig. 10a), the middle of the clouds (Fig. 10b), and the cloud base (Fig. 10c).

These findings are underlined by corresponding plots of the vertical profiles of integrated cloud microphysical properties such as total droplet number concentrations, droplet effective radius, and LWC (Fig. 11). The cloud droplet number concentrations were low and continued to decrease further with height due to coalescence in the clean clouds (see Fig. 11a). These features are opposite in the polluted case due to suppressed coalescence (Fig. 11b). The vertical profiles of the droplet effective radius illustrate that the cloud droplets grow quickly with height for the clean clouds, and vice versa grow slowly with height for the polluted case (see Fig. 11c and Fig. 11d). The LWC plots give evidence that rain develops above 2.7 km above ground in the clean clouds (open red diamonds in Fig. 11e), and that rain is completely suppressed at least up to 6 km altitude in polluted clouds (see Fig. 11f).

b. Remote sensing of cloud thermodynamic phase

The vertical distribution of the thermodynamic phase is directly linked to the formation of precipitation. Therefore, specMACS observed the cloud sides to identify the depth of the mixed–phase layer. The measurement setup applied for the observations of spectral solar radiation reflected from cloud sides using the imaging spectrometers of specMACS is illustrated in Fig. 12. HALO passes a cloud and specMACS observes a vertical column of pixels and records the spectral radiances reflected by the cloud. In this way specMACS takes a series of consecutive snapshots of the reflected spectral solar radiances in the pixel column during the fly–by, which are then used to reconstruct spectral reflected radiance maps of the cloud side. The changes of the roll angle of the aircraft during the fly–by are obvious in Fig. 12. The potential of such cloud side observations of reflected solar radiances using specMACS is exemplified in Fig. 13. In a first step, a cloud mask excludes shaded areas of the cloud from further analysis (grey colored areas in Fig, 13a). Then the spectral slope of the reflected radiance measurements at 1.55 μm and 1.7 μm for each

pixel of the 2D image is calculated, from which a phase index is derived as described by Jäkel et al. (2013). Negative values of the phase index indicate liquid water droplets; positive values hint at ice crystals. Figure 13a shows a corresponding 2D image of the phase index corrected with respect to the flight attitude. The transition between liquid water and ice thermodynamic phases is well defined by the vertical distribution (approximated by the elevation) of the phase index as shown in Fig. 13b. The separation between lower–level liquid water and upper–level ice portions of the convective cloud and thus the vertical extension of the mixed–phase layer is characterized by a strong increase of the phase index from negative to positive values. Stereogrammetry methods have been applied to determine the height of the mixed–phase layer. The analyzed example shown in Figs. 12 and 13 exhibits a mixed–phase layer between 5.5 and 7.6 km altitude, which corresponds to a temperature range of $-3\,^{\circ}$C to $-11\,^{\circ}$C.

c. Cloud microphysical in–situ measurements in cold clouds

Figure 14 shows an example of data from the PHIPS–HALO instrument. The left panel shows results from measurements collected in ambient in–situ cirrus, the right panel contains data sampled in an anvil outflow. The in–situ cirrus was probed at an altitude of 12 km in a temperature below –40 °C. The outflow was sampled also at an altitude of 12 km, with a temperature of –47 °C. So both cases were sampled approximately at the same temperatures, but show different ice crystal habits. This indicates that the formation of the ice crystal took place at different temperatures, i.e. the outflow ice particles have been transported from below, but measured at the cirrus temperature range. It further demonstrates that the microphysical properties of ice particles in anvil outflows of convective cloud systems differ significantly from those of ambient in–situ cirrus. While in–situ cirrus is dominated by small ice particles, bullet rosettes, and bullet rosette aggregates, anvil outflows were largely composed of plates and plate–aggregates. This result clearly reflects the strong

vertical transport that is prevailing in tropical convective systems. Plate–like ice crystals that were heterogeneously nucleated on solid aerosol particles and grown in the lower, warmer parts of the system (warmer than $-37\,^{\circ}$C) were lifted to the cold outflows (colder than $-50\,^{\circ}$C) where they are mixed with in–situ grown columnar crystals. In conjunction with cloud process modeling, the statistical analysis of plate–like ice crystals in the cold outflows can be used to understand the effect of pollution on the dynamics in convective systems.

d. Cloud Condensation Nuclei (CCN)

The number concentration of CCN was measured using a two–column continuous–flow streamwise thermal gradient CCN counter (CCN–200, Droplet Measurement Technologies [DMT] Inc., Boulder, CO, USA). The pressure in the instrument was kept constant at 270 hPa with a specially developed constant pressure inlet, connected to the HASI inlet. To illustrate the CCN data obtained during ACRIDICON–CHUVA, the time series of CCN concentration at a supersaturation of S=(0.53$\pm$0.02) % and the aircraft flight altitude are plotted in Fig. 15. These data were collected in clear air outside of clouds. The measurements were performed downwind of Manaus in the region over Manacapuru, at altitudes from about 1 km to about 13 km (flight AC08, on 09 September 2014). The green markers represent the CCN concentration (interpolated to the same supersaturation) measured at the ground–based measurement station at Manacapuru (T3), which were collected as part of the GoAmazon 2014/5 campaign (data from ARM database: https://www.arm.gov/, see also (Martin et al. 2015)). The CCN measurements taken when HALO was flying in the boundary layer near the ground station are in good agreement with the ground–based CCN measurements at T3.

The mean value and the standard deviation of the CCN concentration in the boundary layer up to about 2 km altitude are (543$\pm$251) cm^{-3}, indicating the presence of pollution–derived aerosol

particles originating from the Manaus area. No strong peaks of CCN concentrations were observed, which suggests rapid aging and distribution of local emissions. Above the boundary layer, CCN concentrations declined to a minimum at around 5 km altitude, and then increased again in the upper troposphere. The origin of these upper tropospheric aerosols is still uncertain: they may be the result of long-range transport at high altitudes or they may have been produced in cloud outflows.

e. Trace gas data

Figure 16 displays vertical profiles of the mixing ratios of O_3, NO_2, NO_y (= NO, NO_2, NO_3, HNO_3,...), CO, and HCHO measured during the northern and southern legs of flight AC11 on 16 September 2014. Here the elevated mixing ratios of NO_2, NO_y, CO, and HCHO detected during the southern leg (open red circles), as compared to the northern leg (open blue diamonds) are indicative of conditions affected by biomass burning (Crutzen and Andreae 1990). The trace gases, NO_2, NO_y, CO, and HCHO, are either directly emitted by biomass burning (CO, NO, and HCHO), or produced by photo–oxidation within the biomass burning plume (NO_2, NO_y, CO, and HCHO). In fact, the visual observations made from the aircraft during AC11 indicated several massive biomass burning plumes in the southern part of the State of Amazonas, and virtually none in the northern part of Amazonas and southern part of Roraima. The measured trace gases will allow to infer emission ratios of some key pollutants from biomass burning as well as studies on aging and photochemical processing of the investigated air masses. The elevated mixing ratios of the pollutants up to the top of the boundary layer (around 950 m) are due to the Manaus city plume.

6. Summary

The ACRIDICON–CHUVA campaign was successfully performed in an area spanning across most of the Amazon basin in September and October 2014. The campaign aimed at studying the evolution of tropical convective clouds over the Brazilian rainforest, and at investigating related interactions with aerosol particles and trace gases by a combination of dedicated airborne and ground–based, in–situ, and remote sensing measurements. Ground–based stations and the new German research aircraft HALO measured the atmospheric and cloud properties in concert with the meteorological, aerosol, and radiative properties, and some key trace gases. This paper gives an overview of the scientific motivation and objectives of the ACRIDICON–CHUVA campaign with a focus on the airborne observations with HALO. Furthermore, the instrumentation and flight patterns of HALO are introduced. HALO proved to be a valuable research tool, carrying a comprehensive scientific payload, flying across much of the Amazon basin, and reaching 15 km flight altitude. A particular advantage of HALO is its extended endurance of up to eight hours, which allowed to flexibly adjust flight patterns to the actual cloud situations.

Some selected measurement results are presented. They indicate the scientific potential of the collected in–situ and remote sensing observations to characterize the evolution of vertical profiles of cloud microphysical parameters, in combination with concurrent aerosol and trace gas measurements. The impact of environmental pollution on the cloud droplet size distribution and its vertical dependence was quantified, showing more small and fewer large cloud droplets in polluted conditions and the related suppression of precipitation. First results of a new spectral imaging technique observing cloud side reflection of solar radiation showed promising results in distinguishing between liquid water droplets and ice crystals. This method shall be further developed to deliver droplet/ice crystal sizes as a function of altitude and cloud temperature in order to reveal typical

signatures in the evolution of tropical convective clouds. Elevated CCN concentrations at higher altitudes were identified; their origin will have be investigated in future work. The characteristics of ice crystals in the outflow were studied and compared with natural cirrus cloud properties. Vertical transport processes were identified by profile measurements of trace gases.

The reader is invited to visit the ACRIDICON-CHUVA website at http://www.uni-leipzig.de/~meteo/acridicon-chuva/. The data are stored in the HALO data base (https://halo-db.pa.op.dlr.de/), which also describes the access to the measurement results. The general data policy is defined in a protocol available at http://www.uni-leipzig.de/~meteo/acridicon-chuva/DataProtocol.html.

This paper reports preliminary results and it marks just the beginning of the detailed data analysis. It is intended to serve as a reference for a series of detailed scientific publications planned for the future.

Acknowledgments. This work was supported by the Max Planck Society, the DFG (Deutsche Forschungsgemeinschaft, German Research Foundation) Priority Program SPP 1294, the German Aerospace Center (DLR), the FAPESP (São Paulo Research Foundation) grants 2009/15235-8 and 2013/05014-0, and a wide range of other institutional partners. The ACRIDICON–CHUVA campaign was carried out in collaboration with the USA–Brazilian atmosphere research project GoAmazon2014/5, including numerous institutional partners. We would like to thank Instituto Nacional de Pesquisas da Amazônia (INPA) for the local logistic help prior, during and after the campaign. Thanks also to the Brazilian Space Agency (AEB: Agência Espacial Brasileira) responsible for the program of cooperation (CNPq license 00254/2013–9 of the Brazilian National Council for Scientific and Technological Development). A special thanks to the DLR Flight Ex-

periments team and pilots. We appreciate the support of the colleagues from *enviscope GmbH* for their valuable help in certifying and installing the numerous instruments for HALO.

References

Albrecht, R. I., C. A. Morales, and M. A. F. S. Dias, 2011: Electrification of precipitating systems over the Amazon: Physical processes of thunderstorm development. *J. Geophys. Res.*, **116**, D08 209, doi:10.1029/2010JD014 756.

Anderson, N., C. Grainger, and J. Stith, 2005: Characteristics of strong updrafts in precipitation systems over the Central Tropical Pacific Ocean and in the Amazon. *J. Appl. Meteor.*, **44**, 731–738.

Andreae, M. O., D. Rosenfeld, P. Artaxo, A. A. Costa, G. P. Frank, K. M. Longo, and M. A. F. Silva-Dias, 2004: Smoking rain clouds over the Amazon. *Science*, **303 (5662)**, 1337–1342, doi:10.1126/science.1092779.

Andreae, M. O., and Coauthors, 2015: The Amazon Tall Tower Observatory (ATTO): overview of pilot measurements on ecosystem ecology, meteorology, trace gases, and aerosols. *Atmos. Chem. Phys.*, **15 (18)**, 10 723–10 776, doi:10.5194/acp-15-10723-2015, URL http://www.atmos-chem-phys.net/15/10723/2015/.

Artaxo, P., and Coauthors, 2002: Physical and chemical properties of aerosols in the wet and dry seasons in Rondônia, Amazonia. *J. Geophys. Res.*, **107**, 8081, doi:10.1029/2001JD000666.

Baidya Roy, S., 2009: Mesoscale vegetation–atmosphere feedbacks in Amazonia. *J. Geophys. Res.*, **114**, D20 111, doi:10.1029/2009JD012001.

Bierwirth, E., and Coauthors, 2009: Spectral surface albedo over Morocco and its impact on the radiative forcing of Saharan dust. *Tellus*, **61B**, 252–269.

631 Buchholz, B., A. Afchine, and V. Ebert, 2014a: Rapid, optical measurement of the atmospheric
632 pressure on a fast research aircraft using open-path TDLAS. *Atmos. Meas. Technol.*, 3653–3666,
633 doi:10.5194/amt–7–3653–2014.

634 Buchholz, B., N. Böse, and V. Ebert, 2014b: Absolute validation of a diode laser hygrometer
635 via intercomparison with the German national primary water vapor standard. *Appl. Phys. B*,
636 883–899, doi:10.1007/s00 340–014–5775–4.

637 Chagnon, J. J. F., and R. L. Bras, 2005: Contemporary climate change in the Amazon. *Geophys.*
638 *Res. Lett.*, **32**, L13 703, doi:10.1029/2005GL022722.

639 Chang, D., and Coauthors, 2015: Comprehensive mapping and characteristic regimes of aerosol
640 effects on the formation and evolution of pyro–convective clouds. *Atmos. Chem. Phys.*, **15**,
641 10 325–10 348, doi:10.5194/acp-15-10325-2015.

642 Crutzen, P. J., and M. O. Andreae, 1990: Biomass burning in the tropics: Impact on atmospheric
643 chemistry and biogeochemical cycles. *Science*, **250**, 1669–1678, doi:10.1126/science.250.4988.
644 1669.

645 Cutrim, E., D. W. Martin, and R. Rabin, 1995: Enhancement of cumulus clouds over deforested
646 lands in Amazonia. *Bull. Amer. Meteorol. Soc.*, **76**, 1801–1805.

647 Dahlkötter, F., and Coauthors, 2014: The Pagami Creek smoke plume after long-range transport to
648 the upper troposphere over Europe – aerosol properties and black carbon mixing state. *Atmos.*
649 *Chem. Phys.*, **14**, 6111–6137, doi:10.5194/acp–14–6111–2014.

650 DeMott, P., and Coauthors, 2010: Predicting global atmospheric ice nuclei distributions and their
651 impacts on climate. *PNAS*, **107**, 11 217–11 222.

652 Despres, V. R., and Coauthors, 2012: Biological aerosol particles in the atmosphere: A review.
653 *Tellus B*, **64**, 15 598, doi:10.3402/tellusb.v64i0.15598.

654 Drewnick, F., and Coauthors, 2005: A new time–of–flight aerosol mass spectrometer (ToF-AMS)
655 – instrument description and first field deployment. *Aerosol Sci. Technol.*, **39**, 637–658.

656 Durieux, L., L. Machado, and H. Laurent, 2003: The impact of deforestation on cloud cover over
657 the Amazon arc of deforestation. *Remote Sens. Environ.*, **86**, 132–140.

658 Ehrlich, A., E. Bierwirth, M. Wendisch, J.-F. Gayet, G. Mioche, A. Lampert, and J. Heintzen-
659 berg, 2008: Cloud phase identification of arctic boundary-layer clouds from airborne spectral
660 reflection measurements: Test of three approaches. *Atmos. Chem. Phys.*, **8**, 7493–7505.

661 Ewald, F., T. Kölling, A. Baumgartner, T. Zinner, and B. Mayer, 2015: Design and char-
662 acterization of specMACS, a multipurpose hyperspectral cloud and sky imager. *Atmos.*
663 *Meas. Technol. Discuss.*, **8 (9)**, 9853–9925, doi:10.5194/amtd-8-9853-2015, URL http://www.
664 atmos-meas-tech-discuss.net/8/9853/2015/.

665 Fan, J., L. R. Leung, D. Rosenfeld, Q. Chen, Z. Li, J. Zhang, and H. Yan, 2013: Mi-
666 crophysical effects determine macrophysical response for aerosol impacts on deep convec-
667 tive clouds. *Proceedings of the National Academy of Sciences*, **110 (48)**, E4581–E4590,
668 doi:10.1073/pnas.1316830110, URL http://www.pnas.org/content/110/48/E4581.abstract, http:
669 //www.pnas.org/content/110/48/E4581.full.pdf.

670 Fan, J., D. Rosenfeld, Y. Ding, L. R. Leung, and Z. Li, 2012: Potential aerosol indirect effects
671 on atmospheric circulation and radiative forcing through deep convection. *Proceedings of the*
672 *National Academy of Sciences*, **39 (9)**, L09 806, doi:10.1029/2012GL051851.

673 Fan, J., and Coauthors, 2009: Dominant role by vertical wind shear in regulating aerosol effects
674 on deep convective clouds. *J. Geophys. Res.*, **114**, D22 206, doi:10.1029/2009JD012352.

675 Fisch, G., J. Tota, L. A. T. Machado, M. A. F. Dias, L. F. Silva, and C. Nobre, 2004: The convective
676 boundary layer over pasture and forest in Amazonia. *Theor. Appl. Climatology*, **78**, 47–60.

677 Gonçalves, W. A., L. A. T. Machado, and P.-E. Kirstetter, 2014: The biomass burning aerosol
678 influence on precipitation over the Central Amazon: an observational study. *Atmos. Chem. Phys.*
679 *Discuss.*, **14**, 18 879–18 904, doi:10.5194/acpd-14-18879-2014.

680 Gunthe, S. S., and Coauthors, 2009: Cloud condensation nuclei in pristine tropical rainforest air
681 of amazonia: Size–resolved measurements and modeling of atmospheric aerosol composition
682 and ccn activity. *Atmos. Chem. Phys.*, **9**, 7551–7575.

683 Hallett, J., and S. C. Mossop, 1974: Production of secondary ice particles during riming process.
684 *Nature*, **249 (5452)**, 26–28.

685 Heintzenberg, J., and R. J. Charlson, 2009: *Clouds in the perturbed climate system - Their rela-*
686 *tionship to energy balance, atmospheric dynamics, and precipitation*. MIT Press, Cambridge,
687 UK, 58-72 pp.

688 Heymsfield, A., A. Bansemer, P. Field, S. Durden, J. Stith, J. Dye, W. Hall, and C. Grainger,
689 2002: Observations and parameterizations of particle size distributions in deep tropical cirrus
690 and stratiform precipitating clouds: Results from in–situ observations in TRMM field cam-
691 paigns. *J. Atmos. Sci.*, **59**, 3457–3491.

692 Horel, J. D., A. N. Hahmann, and J. E. Geisler, 1989: An investigation of the annual cycle of the
693 convective activity over the tropical americas. *J. Climate*, **2 (11)**, 1388–1403.

Jäkel, E., J. Walther, and M. Wendisch, 2013: Thermodynamic phase retrieval of convective clouds: impact of sensor viewing geometry and vertical distribution of cloud properties. *Atmos. Meas. Tech.*, **6**, 539–547, doi:10.5194/amt-6-539-2013.

Khain, A. P., N. Benmoshe, and A. Pokrovsky, 2008: Factors determining the impact of aerosols on surface precipitation from clouds: An attempt at classification. *J. Atmos. Sci.*, **65**, 1721–1748, doi:10.1175/2007JAS2515.1.

Khain, A. P., L. R. Leung, B. Lynn, and S. Ghan, 2009: Effects of aerosols on the dynamics and microphysics of squall lines simulated by spectral bin and bulk parameterization schemes. *J. Geophys. Res.*, **114**, D22 203, doi:10.1029/2009JD011902.

Kolb, C. E., and Coauthors, 2010: An overview of current issues in the uptake of atmospheric trace gases by aerosols and clouds. *Atmos. Chem. Phys.*, **10**, 10 561–10 605, doi:10.5194/acp-10-10561-2010.

Krüger, M. L., and Coauthors, 2014: Assessment of cloud supersaturation by size–resolved aerosol particle and cloud condensation nuclei (CCN) measurements. *Atmos. Meas. Technol.*, **7**, 2615–2629, doi:10.5194/amt-7-2615-2014.

Laursen, K. K., D. P. Jorgensen, G. P. Brasseur, S. L. Ustin, and J. R. Huning, 2006: HIAPER: The next generation NSF/NCAR research aircraft. *Bull. Amer. Meteorol. Soc.*, **87**, 896–909, doi:10.1175/BAMS–87–7–896.

Lebo, Z. J., and H. Morrison, 2014: Dynamical effects of aerosol pertubations on simulated idealized squall lines. *Mon. Wea. Rev.*, **142**, 991–1009, doi:10.1175/MWR-D-13-00156.1.

Li, Z. Q., F. Niu, J. W. Fan, Y. G. Liu, D. Rosenfeld, and Y. N. Ding, 2011: Long-term impacts of aerosols on the vertical development of clouds and precipitation. *Nature Geoscience*, **4 (12)**, 888–894, doi:10.1038/NGEO1313.

Machado, L. A. T., and Coauthors, 2014: The CHUVA project: How does convection vary across Brazil. *Bull. Amer. Meteorol. Soc.*, doi:10.1175/BAMS-D-13-00084.1.

Martin, S. T., and Coauthors, 2010: Sources and properties of Amazonian aerosol particles. *Rev. Geophys.*, **48**, RG2002, doi:10.1029/2008RG000280.

Martin, S. T., and Coauthors, 2015: Introduction: Observations and modeling of the Green Ocean Amazon (GoAmazon2014/5). *Atmos. Chem. Phys. Discuss.*, **15**, 30 175–30 210, www.atmos–chem–phys–discuss.net/15/30 175/2015/, doi:10.5194/acpd-15-30175-2015.

Morrison, H., and W. W. Grabowski, 2013: Response of tropical deep convection to localized heating pertubations: Implications for aerosol–induced convective invigoration. *J. Atmos. Sci.*, **70**, 3533–3555, doi:10.1175/JAS-D-13-027.1.

Negri, A., R. Adler, L. Xu, and J. Surrat, 2004: The impact of Amazonian deforestation on dry season rainfall. *J. Climate*, **17**, 1306–1319.

Neves, A. T., and G. Fisch, 2015: The daily cycle of the atmospheric boundary layer heights over pasture site in Amazonia. *Am. J. Environm. Engineering*, **5**, 39–44, doi:10.5923/s.ajee.201 501.06.

Paramonov, M., and Coauthors, 2015: A synthesis of cloud condensation nuclei counter (CCNC) measurements within the EUCAARI network. *Atmos. Chem. Phys.*, **15**, 12 211–12 229, doi: 10.5194/acp-15-12211-2015.

735 Platt, U., and J. Stutz, 2008: *Differential Optical Absorption Spectroscopy: Principles and Appli-*
736 *cations*. Series: Physics of Earth and Space Environments, Springer Verlag, ISBN: 3540211934.

737 Pöschl, U., and Coauthors, 2010: Rainforest aerosols as biogenic nuclei of clouds and precipitation
738 in the amazon. *Science*, **429**, 513–1516.

739 Reutter, P., and Coauthors, 2009: Aerosol– and updraft–limited regimes of cloud droplet forma-
740 tion: influence of particle number, size and hygroscopicity on the activation of cloud condensa-
741 tion nuclei (CCN). *Atmos. Chem. Phys.*, **9**, 7067–7080.

742 Roberts, G. C., A. Nenes, J. H. Seinfeld, and M. O. Andreae, 2003: Impact of biomass
743 burning on cloud properties in the Amazon Basin. *J. Geophys. Res.*, **108 (D2)**, 4062, doi:
744 10.1029/2001JD000985.

745 Rosenfeld, D., 1999: TRMM observed first direct evidence of smoke from forest fires inhibiting
746 rainfall. *Geophys. Res. Lett.*, **26**, 3105–3108.

747 Rosenfeld, D., and I. M. Lensky, 1998: Satellite-based insights into precipitation formation pro-
748 cesses in continental and maritime convective clouds. *Bull. Amer. Meteor. Soc.*, **79 (11)**, 2457–
749 2476.

750 Rosenfeld, D., U. Lohmann, G. B. Raga, C. D. O'Dowd, M. Kulmala, S. Fuzzi, A. Reissell,
751 and M. O. Andreae, 2008: Flood or drought: How do aerosols affect precipitation? *Science*,
752 **321 (5894)**, 1309–1313.

753 Rosenfeld, D., and Coauthors, 2014: Global observations of aerosol-cloud-precipitation-climate
754 interactions. *Reviews of Geophysics*, **52 (4)**, 750–808, doi:10.1002/2013RG000441, URL http:
755 //dx.doi.org/10.1002/2013RG000441, 2013RG000441.

Schmale, J., and Coauthors, 2010: Aerosol layers from the 2008 eruptions of Mt. Okmok and Mt. Kasatochi: In-situ UT/LS measurements of sulfate and organics over Europe. *J. Geophys. Res.*, doi:10.1029/2009JD013628.

Shukla, J., C. Nobre, and P. Sellers, 1990: Amazon deforestation and climate change. *Science*, **247**, 1322–1325.

Silva Dias, M. A. F., and Coauthors, 2002: Cloud and rain processes in a biosphere-atmosphere interaction context in the Amazon region. *J. Geophys. Res.*, **107 (D20)**, LBA 39–1–LBA 39–18, doi:10.1029/2001JD000335, URL http://dx.doi.org/10.1029/2001JD000335, 8072.

Stith, J., J. Fye, A. Bansemer, A. Heymsfield, C. Grainger, W. Petersen, and R. Cifelli, 2002: Microphysical observations of tropical clouds. *J. Appl. Meteorol.*, **41**, 97–117.

Tao, W.-K., J.-P. Chen, Z. Li, C. Wang, and C. Zhang, 2012: Impact of aerosols on convective clouds and precipitation. *Reviews of Geophysics*, **50 (2)**, 1–62, doi:10.1029/2011RG000369, URL http://dx.doi.org/10.1029/2011RG000369, rG2001.

Wang, C., and R. Prinn, 2000: On the roles of deep convective clouds in tropospheric chemistry. *J. Geophys. Res.*, **105 (D17)**, 22 269–22 297.

Wang, J., and Coauthors, 2010: Impact of deforestation in the Amazon basin on cloud climatology. *PNAS*, **106**, 3670–3674, doi:www.pnas.org/cgi/do/10.1073/pnas.0810156106.

Wendisch, M., and J.-L. Brenguier, 2013: *Airborne Measurements for Environmental Research – Methods and Instruments*. Wiley–VCH Verlag GmbH & Co. KGaA, Weinheim, Germany, Weinheim, Germany, 354 pp., iSBN: 978-3-527-40996-9.

Wendisch, M., D. Müller, D. Schell, and J. Heintzenberg, 2001: An airborne spectral albedometer with active horizontal stabilization. *J. Atmos. Oceanic Technol.*, **18 (11)**, 1856–1866.

778 Williams, E., and Coauthors, 2002: Contrasting convective regimes over the Amazon: Impli-
779 cations for cloud electrification. *J. Geophys. Res.*, **107 (D20)**, LBA 50–1–LBA 50–19, doi:
780 10.1029/2001JD000380, URL http://dx.doi.org/10.1029/2001JD000380.

781 Zheng, Y., and D. Rosenfeld, 2015: Linear relation between convective cloud base height and
782 updrafts and application to satellite retrievals. *Geophys. Res. Lett.*, **42**, 6485–6491.

LIST OF TABLES

TABLE 1. Instrumentation installed on the HALO aircraft during the ACRIDICON–CHUVA campaign. The acronyms are explained in Table 3. λ is the symbol for wavelength, ν for frequency, D_p indicates the particle diameter, T the temperature, and S the supersaturation. Additional references are given in brackets: [1] Buchholz et al. (2014a), [2] Buchholz et al. (2014b), [3] Drewnick et al. (2005), [4] Schmale et al. (2010), [5] Platt and Stutz (2008), [6] Dahlkötter et al. (2014), [7] Ewald et al. (2015), [8] Wendisch et al. (2001), [9] Ehrlich et al. (2008), [10] Bierwirth et al. (2009).

Instrument Acronym [Additional Reference]	Measured Quantity	R: Range of Measurement P: Precision, A: Accuracy	Time Resolution in Hz
INLETS			
HALO–CVI	Inlet for cloud particles and residues	D_p = 5–50 μm	
HASI	HALO Aerosol Submicrometer Inlet	D_p up to a few μm (analysis ongoing)	
TGI	Trace Gas Inlet		
METEOROLOGY			
BAHAMAS	Pressure, temperature, wind, humidity, TAS		Up to 100
	Aircraft position, attitude, heading, altitude		
BAHAMAS-SHARC	H_2O mixing ratio (gas phase)	R: 20-60,000, A: $<$ 10 %	1
MTP	Microwave radiances for temperature profiles	R: ν = 56.363, 57.612, 58.363 GHz	0.1
HAI [1,2]	H_2O Gas phase concentration	R: 1–40,000 ppmv (Vapor)	up to 120
	4 channels: 2 $\times$ open–path, 2 $\times$ closed–path	A: 4.3 %	
CHEMISTRY			
Aerosol Impactor	Collects aerosol particles for microspectroscopy	R: $>$ 100 nm	Offline Analysis
C–ToF–AMS [3,4]	Non–refractory particle composition	R: D_p = 40 nm–1 μm, A & P: $\approx$ 30 %	0.03
	(organics, sulfate, nitrate, ammonium, chloride)		
AMTEX	CO, O_3 concentrations	P: 2 ppb; A: 5 %	1
	PFCs (C_6F_{12}, C_7F_{14})	P: 1 ppq; A: 3 %	1
ITMS	PAN (PeroxyAcetyl Nitrate), SO_2–concentration	P: 5 ppt; A: 7 %	1
	HNO_3, HONO concentrations	P: 30 ppt; A: 10 %	1
PERTRAS	PFCs: Perfluorocarbons		
AENEAS	NO, NO_y	R: 5 pmol/mol–60 nmol/mol	1
		NO: A: $\sim$8 % at 50 nmol/mol	
		NO_y: A: $\sim$7 % at 450 nmol/mol	
miniDOAS [5]	Spectral radiance to derive trace gas concen–	R: λ = 310–1680 nm; $\Delta\lambda$=0.7–7 nm	10
	trations: HCHO, BrO, IO, ClO_2, $C_2H_2O_2$, CH_4		
	BrO_2, I_2, O_2, O_3, O_4, NO_2, HONO, H_2O, CO_2		

Instrument Acronym [Additional Reference]	Measured Quantity	R: Range of Measurement P: Precision, A: Accuracy	Time Resolution in Hz
MICROPHYSICS			
Aerosol Particles			
SNOOPY (SP2) [6]	rBC mass/number concentration, aerosol PSD	R: rBC Mass: 0.26–125 fg (65–510 nm)	1
AMETYST			
– CPC	Particle number concentration	R: D_p = 5 nm–1 μm	1
– PSAP	Particle absorption coefficient	R: λ = 467, 530, 660 nm	1
– DMPS & OPC	Aerosol PSD	R: D_p = 5–350 nm & 250 nm–3 μm	1
Permanently Behind CVI			
– CPC	Residual particle number concentration	R: D_p = 10 nm–3 μm	0.33
– PSAP	Residual particle absorption coefficient	R: λ = 567 nm	0.33
– UHSAS	Residual PSD	R: D_p = 100 nm–1 μm	0.33
– Electrometer	Drop charge		0.33
UHSAS–A	Aerosol PSD	R: D_p = 60 nm–1 μm	1
PCASP-100X	Aerosol PSD	R: D_p = 0.12–3.5 μm	1
CCN and IN			
CCN–200	CCN concentration	R: $S = 0.13 - 0.53$ %	1
FINCH	Total and biological IN concentrations	R: $T \geq -40$ °C, sat. ratio wrt ice ≤ 2	0.1
SP2 [6]	rBC mass concentration, aerosol PSD	R: D_p = 120–360 nm	1
Cloud Particles			
CAS–DPOL	Cloud PSD and shape, Liquid Water Content	R: D_p = 0.5–50 μm	1
PHIPS–HALO	Cloud PSD, stereoscopic particle imaging	R: D_p = 10 μm–1 mm	1
	Single particle scattering phase function		
SID–3	Cloud PSD, ice particle shape,	R: D_p = 5–50 μm	1
	Surface roughness		
NIXE–CAPS			
– CAS–DPOL	Cloud PSD, asphericity	R: D_p = 0.6–50 μm	1
– CIPgs	Cloud PSD	R: D_p = 15–950 μm; ΔD_p = 15 μm	1
CCP			
– CDP	Cloud PSD	R: D_p = 3–50 μm; ΔD_p = 1–2 μm	1
– CIPgs	Cloud PSD	R: D_p = 15–950 μm; ΔD_p = 15 μm	1
Precipitation			
PIP	Precipitation PSD	R: D_p = 100–6400 μm; ΔD_p = 100 μm	1

Instrument Acronym [Additional Reference]	Measured Quantity	R: Range of Measurement P: Precision, A: Accuracy	Time Resolution in Hz
RADIATION			
specMACS [7]	Spectral radiance	R: λ = 400–2500 nm; $\Delta\lambda$=5–10 nm	30–100
SMART [8,9,10]	Spectral irradiance (upward and downward)	R: λ = 350–2200 nm; $\Delta\lambda$=2–16 nm	2
	Spectral radiance (upward, FOV = 2.1°)	R: λ = 350–2200 nm; $\Delta\lambda$=2–16 nm	2

TABLE 2. Summary of flights with HALO performed during the ACRIDICON–CHUVA campaign. The research topics covered and the corresponding flight patterns as introduced in Section 3 are indicated by letters (a)–(e) with: a. Cloud vertical evolution and life cycle (cloud profiling), b. Cloud processing of aerosol particles and trace gases (inflow and outflow), c. Satellite and radar validation (cloud products), d. Vertical transport and mixing (tracer experiment), and e. Cloud formation over forested/deforested areas.

#	Date in 2014	Research Topic	Ceiling Altitude (km)	Time Span (Hours)	Remark
AC07	06 September	a	13.9	07:35	Test of Flight Strategy
AC08	09 September	a	13.8	05:30	Coordinated with G1
AC09	11 September	a	12.6	06:10	Clean Conditions
AC10	12 September	c	14.4	07:25	Along A–Train Path
AC11	16 September	b, d	12.9	07:25	Tracer Experiment
AC12	18 September	a	13.8	06:15	Polluted Conditions
AC13	19 September	a	12.9	06:30	Polluted Conditions
AC14	21 September	c	15.2	07:15	Coordinated with G1 Along A–Train Path
AC15	23 September	c, b	13.8	07:20	Along A–Train Path
AC16	25 September	b, d	13.2	06:50	Tracer Experiment
AC17	27 September	e	8.1	06:40	Comparison with GPM
AC18	28 September	a	14.4	06:50	Clean Conditions
AC19	30 September	a	13.8	07:15	Marine Conditions
AC20	01 October	b, a	14.4	07:05	Coordinated with G1

TABLE 3. List of Abbreviations and Acronyms.

3D	Three–Dimensional
2D	Two–Dimensional
AC	ACRIDICON–CHUVA
ACRIDICON	Aerosol, Cloud, Precipitation, and Radiation Interactions and Dynamics of Convective Cloud Systems
AMAZE	Amazonian Aerosol Characterization Experiment
AENEAS	AtmosphEric Nitrogen oxides mEAsuring System
ARM	Atmospheric Radiation Measurement
AMETYST	Aerosol MEasuremenT SYSTem
AMTEX	Atmospheric Tracer Experiment
asl	Above Mean Sea Level
ATTO	Amazon Tall Tower Observatory
BAHAMAS	BAsic HALO Measurement And Sensor System
BC	Black Carbon
rBC	refractory Black Carbon
CALIPSO	Cloud–Aerosol Lidar and Infrared Pathfinder Satellite Observations
CAPE	Convective Available Potential Energy
CAS–DPOL	Cloud Aerosol Spectrometer with Detector for POLarization
CAPS	Cloud, Aerosol, and Precipitation Spectrometer
CCN	Cloud Condensation Nuclei
CCP	Cloud Combination Probe
CDP	Cloud Droplet Probe
CHUVA	Cloud processes of tHe main precipitation systems in Brazil: A contribUtion to cloud resolVing modeling and to the GPM (Global Precipitation Measurements)
CIP	Cloud Imaging Probe
CPC	Condensation Particle Counter
C–ToF–AMS	Compact Time–of–Flight Aerosol Mass Spectrometer
CVI	Counterflow Virtual Impactor
DMPS	Differential Mobility Particle Sizer
dTDLAS	direct Tunable Diode Laser Absorption Spectroscopy
miniDOAS	miniaturized Differential Optical Absorption Spectroscopy

DSD	Droplet Size Distribution
FOV	Field of View
FINCH	Fast Ice Nuclei Chamber
GoAmazon2014/5	Observations and Modeling of the Green Ocean Amazon
GPM	Global Precipitation Measurements
HAI	Hygrometer for Atmospheric Investigations
HALO	High Altitude and LOng Range research aircraft
HASI	HALO Aerosol Submicrometer Inlet
HIAPER	High–Performance Instrumented Airborne Platform for Environmental Research
IN	Ice Nuclei
INPE	Instituto Nacional de Pesquisas Espaciais
IOP2	Second Intensive Operating Period
ITMS	Ion Trap Mass Spectrometer
LBA	Large Scale Biosphere Atmosphere Experiment in Amazonia
LWC	Liquid Water Content
MODIS	Moderate Resolution Imaging Spectroradiometer
NASA	National Aeronautics and Space Administration
MTP	Microwave Temperature Profiler
NIXE–CAPS	The New Ice eXperimEnt – Cloud Aerosol Precipitation Spectrometer
OPC	Optical Particle Counter
PAN	PeroxyAcetyl Nitrate
PCASP	Passive Cavity Aerosol Spectrometer Probe
PERTRAS	Perfluorocarbon Tracer Measurement System
PFC	Perfluorocarbon
PHIPS–HALO	Particle Habit Imaging and Polar Scattering Probe for HALO
PIP	Precipitation Imaging Probe
PSD	Particle Size Distribution
PSAP	Particle Soot Absorption Photometer

SAMBBA	South AMerican Biomass Burning Analysis
SHARC	Sophisticated Hygrometer for Atmospheric ResearCh
SID–3	Small Ice Detector 3
SLW	Supercooled Liquid Water
SMART	Spectral Modular Airborne Radiation Measurement System
SMOCC	Smoke, Aerosols, Clouds, Rainfall, and Climate
SMPS	Scanning Mobility Particle Sizer
SNOOPY	SiNgle–ParticleSOOtPhotometer SYstem
SP2	Single Particle Soot Photometer
specMACS	cloud spectrometer of Munich Aerosol and Cloud Scanner
TAS	True Air Speed
TD	Thermal Denuder
TDL	Tunable Diode Laser
TGI	Trace Gas Inlet
TRMM	Tropical Rainfall Measuring Mission
TROCCINOX	Tropical Convection and its Impact on the Troposphere and Lower Stratosphere
UHSAS	Ultra–High Sensitivity Aerosol Spectrometer
UHSAS–A	Ultra–High Sensitivity Aerosol Spectrometer–Airborne
UTC	Universal Time Coordinated

LIST OF FIGURES

droplet size distributions shown in Fig. 9. The left panels (a, c, e) show the data from flight AC09 (clean case), and the right panels (b, d, f) from flight AC12 (polluted cloud influenced by biomass burning). In the lowest two panels (e and f) black symbols show the cloud LWC (considering particles with diameter smaller than 50 μm, measured by the CAS–DPOL), red symbols indicate rain LWC (including particles with diameter equal or larger than 50 μm, from CIPgs). The rain is suppressed in the polluted case (panel f). 57

Fig. 12. Cloud–side observations of reflected solar radiances for a cloud during flight AC20. The black vertical line indicates a dark–current measurement. Changes of the elevation angle above/below horizon results from variable roll angles of the aircraft. 58

Fig. 13. Phase index derived from the specMACS measurements of cloud–side reflected radiances for the same cloud as in Fig. 12 (from flight AC20). (a) Time series of vertical distribution of the phase index (side view), recorded during a fly–by. The different colors represent values of the phase index. The dark grey areas indicate cloudless portions or land surface; the light gray areas represent shadow zones of the cloud sides, which are excluded from further analysis by an automatic cloud mask algorithm. These shadowed areas are not suitable for phase index analysis. The black vertical line indicates a dark–current measurement. (b) Vertical profile of phase index; three approximate altitudes (5.5; 7.6; 11.7 km) are allocated to vertical pixels. 59

Fig. 14. Statistical analysis of the ice microphysical properties of ambient in–situ cirrus sampled during flight AC12 and of an anvil outflow of a tropical convective system sampled during flight AC16. The analysis is based on stereoscopic images taken by the PHIPS–HALO probe, which was newly developed for HALO. 60

Fig. 15. Time series plot of CCN concentrations and altitude during flight AC08. The green markers represent the CCN measurements performed at the T3 measurement site near Manacapuru. Particle number concentrations have been normalized to standard air pressure (1000 hPa) and temperature (273.15 K). 61

Fig. 16. Profiles of mixing ratios of O_3 (panel a), NO_2 (panel b), NO_y (panel c), CO (panel d), HCHO (panel e) measured during flight AC11 on 16 September 2014. The southern leg of AC11 was performed under notably more polluted conditions (open red circles) than the northern leg (open blue diamonds). The cluster points indicate the variability of concentrations for individual altitudes measured at constant flight levels. Unfortunately during flight AC11 the NO detection channel was not working. 62

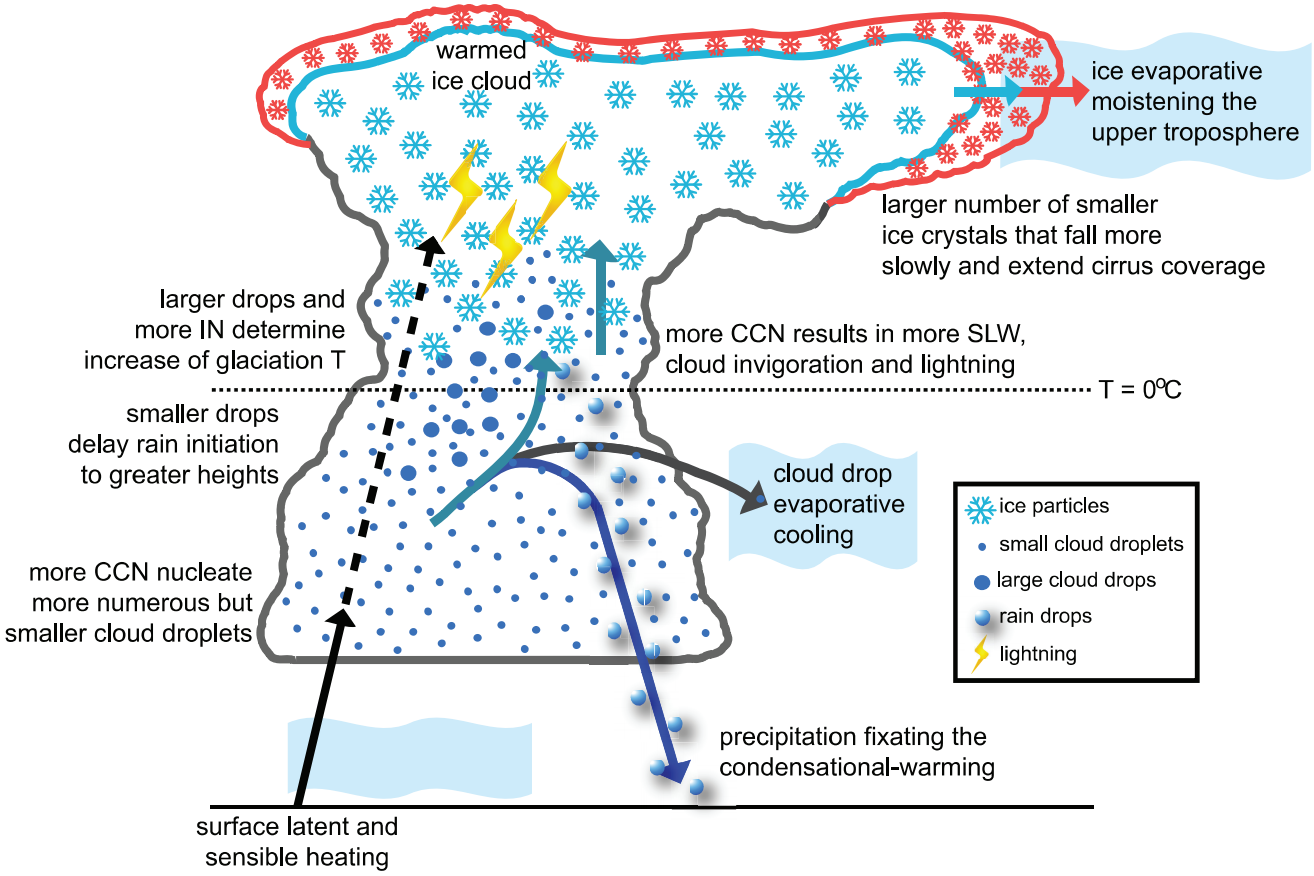

885 FIG. 1. Conceptual diagram of increased Cloud Condensation Nuclei (CCN) effects on deep convective clouds
886 over Amazonia in the dry season. SLW stands for Supercooled Liquid Water, T for temperature.

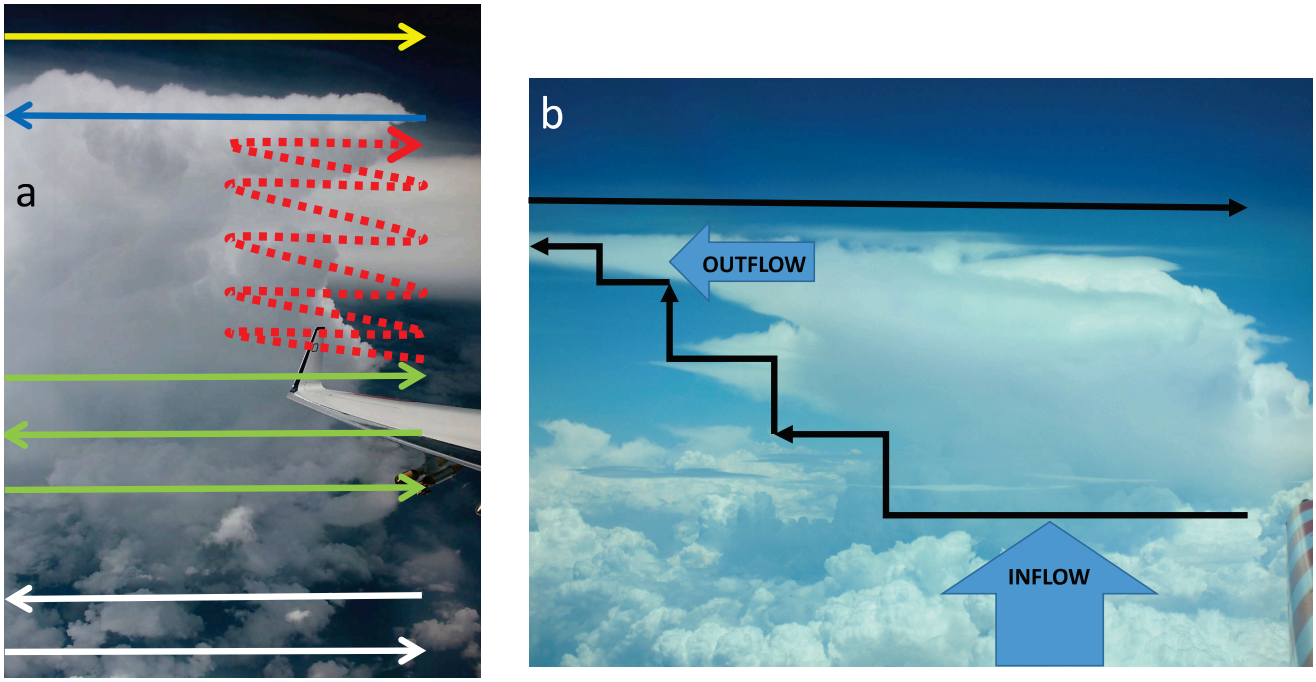

FIG. 2. Schematics of flight patterns for mission types a (left photo, from AC15) and b (right photo, from AC20).

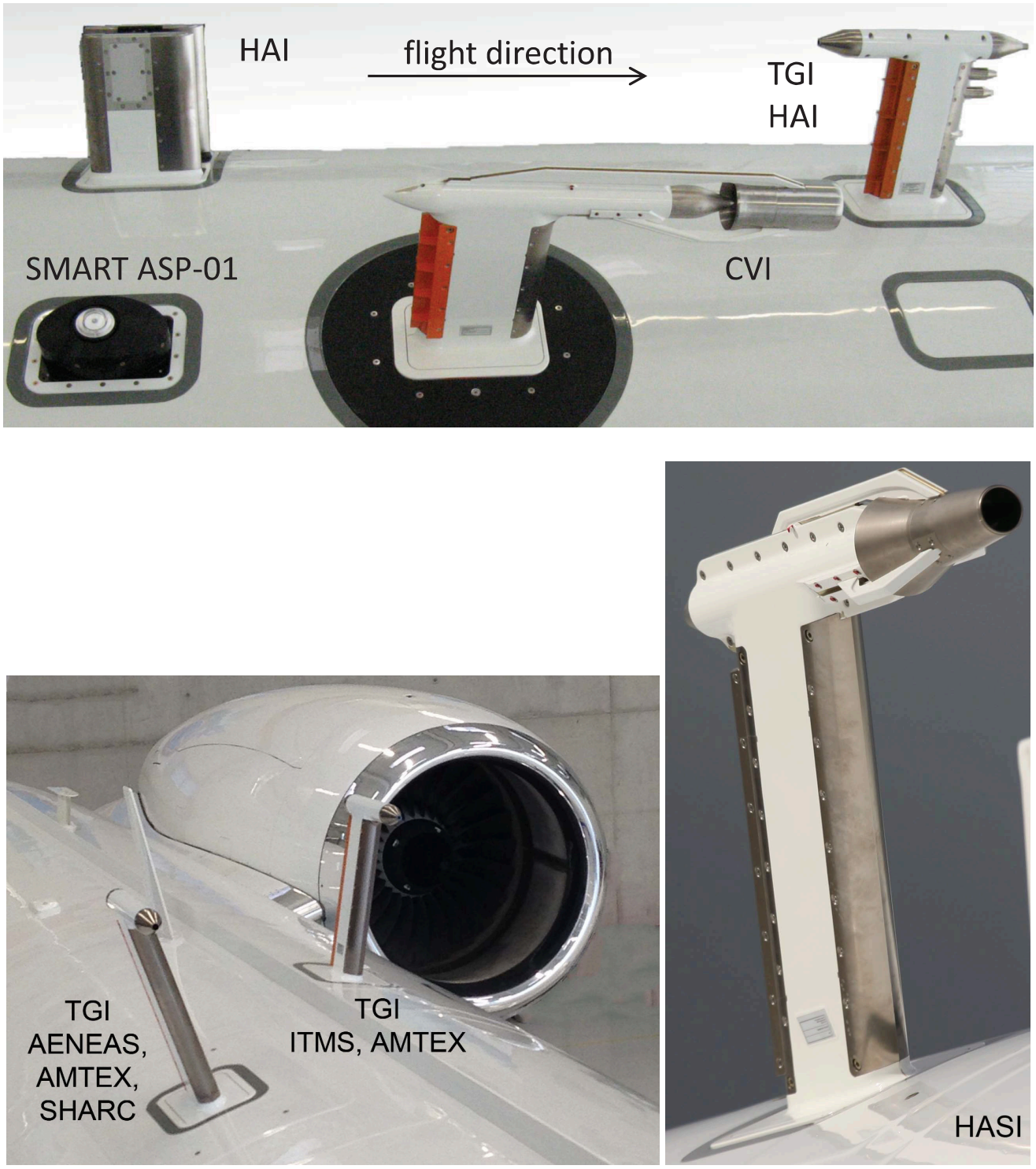

FIG. 3. Photos of parts of the upper fuselage of HALO. Upper panel: Shown are the external structures of the HAI (Hygrometer for Atmospheric Investigations), the TGI (Trace Gas Inlet), and the HALO–CVI (Counterflow Virtual Inlet). The upward looking irradiance optical inlet of the SMART (Spectral Modular Airborne Radiation Measurement System) is also depicted. Lower two panels: The two TGIs (Trace Gas Inlets) and the HASI (HALO Aerosol Submicrometer Inlet) are pictured.

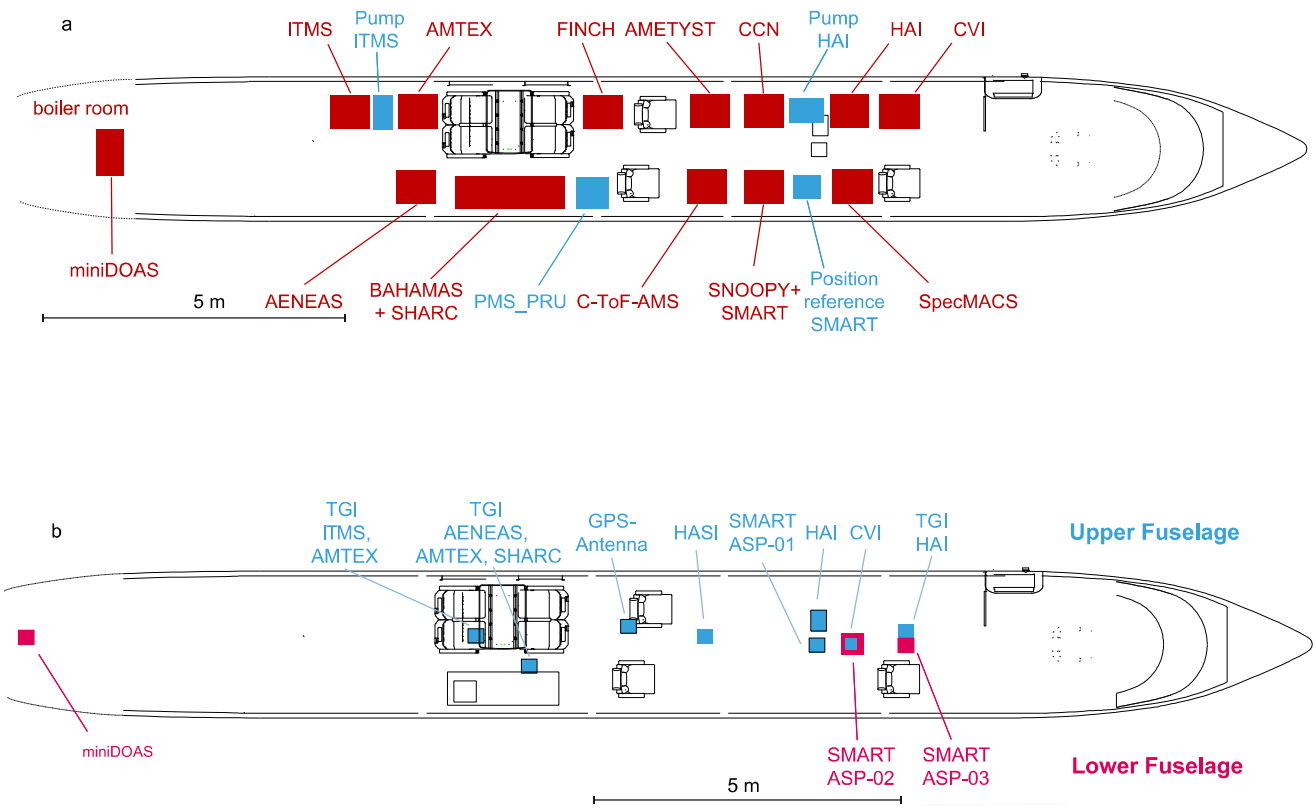

892 FIG. 4. Sketch of the cross section (top view) of HALO. (a) In red the positions of the instrument racks
893 installed in the cabin are indicated. In blue additional technical equipment such as pumps or reference systems
894 are given (PMS_PRU is the major data acquisition for PMS probes). (b) Inlets and apertures mounted/installed
895 on the upper (blue) and lower (red) fuselage.

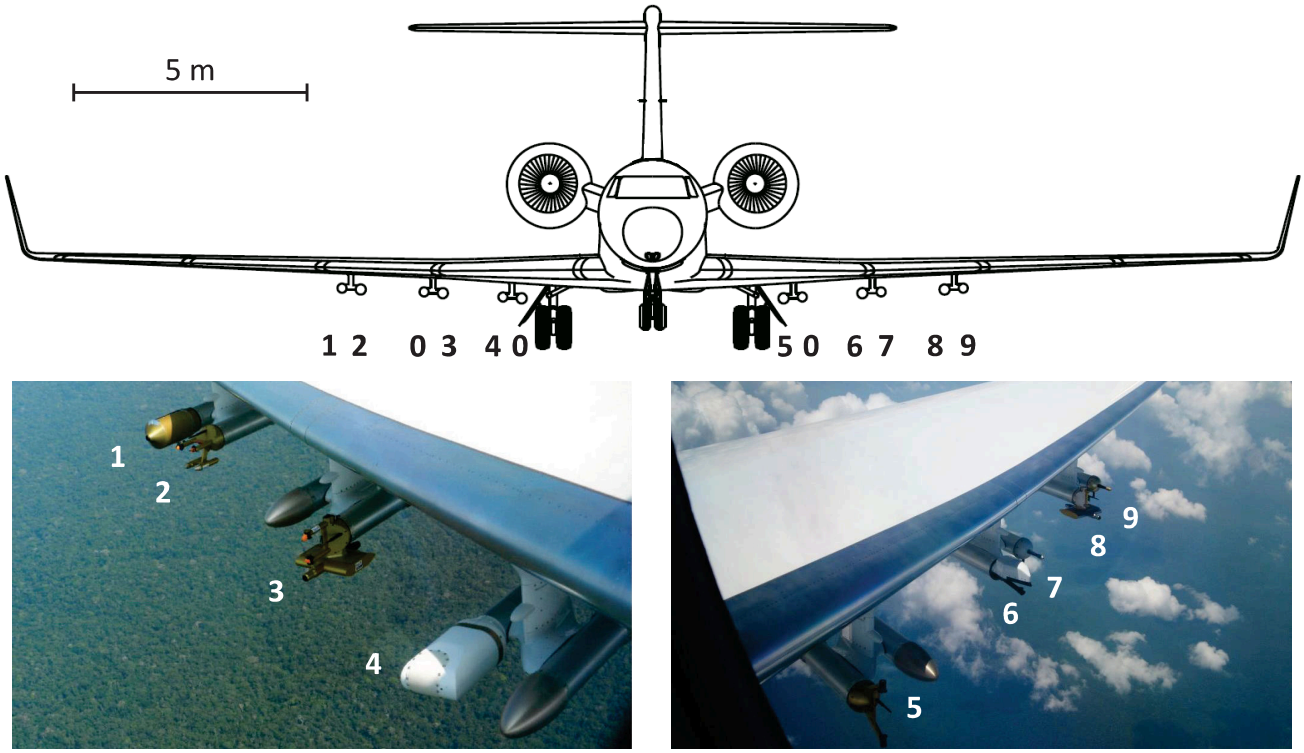

FIG. 5. Sketch of cross section of HALO as viewed from the aircraft nose (upper panel). The numbers indicate the positions of the PMS probes mounted under the wings: 0 Dummy, 1: PHIPS–HALO, 2: CCP, 3: NIXE-CAPS, 4: MTP, 5: PIP, 6: SID-3, 7: PCASP-100X, 8: CAS-DPOL, 9: UHSAS–A. The photos in the lower two panels illustrate the instruments mounted underneath the wings of HALO.

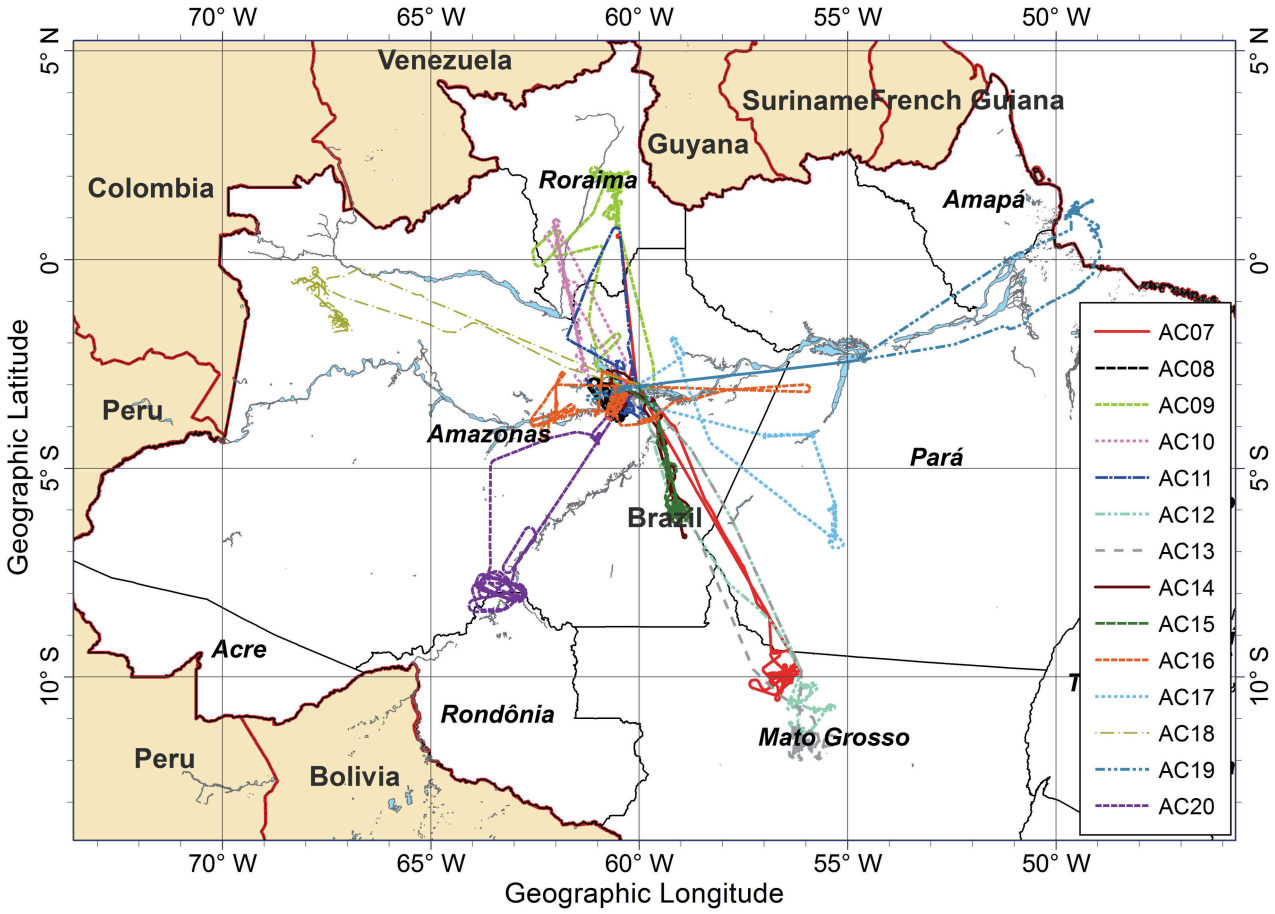

FIG. 6. Flight tracks for all scientific missions (AC07 to AC20).

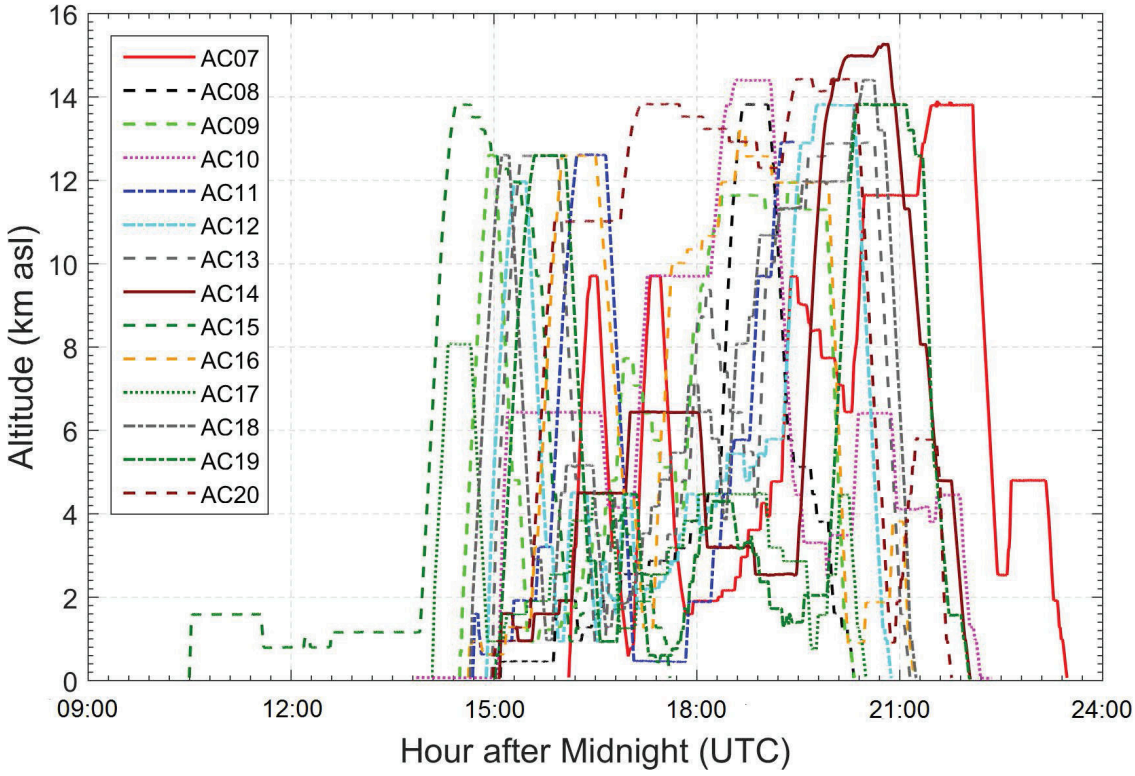

900 FIG. 7. Flight altitude above mean sea level (above sea level, asl) plotted as a function of time (hour after
901 midnight, UTC) for all scientific missions (AC07 to AC20).

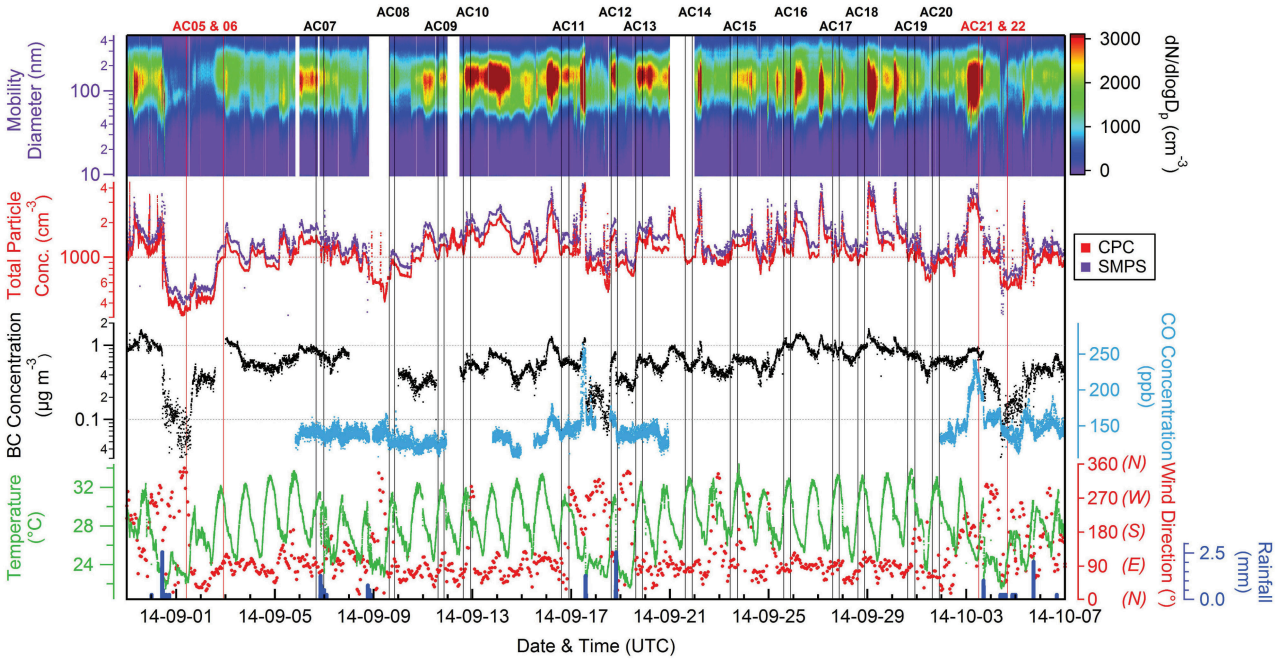

902 FIG. 8. Overview representation of selected time series from long term measurements at the Amazon Tall
903 Tower Observatory (ATTO) site, 150 km northeast of Manaus. The data were taken at 60 m altitude. This site is
904 also referred to as T0a in GoAmazon2014/5. Particle number concentrations have been normalized to standard
905 air pressure (1000 hPa) and temperature (273.15 K). CPC is the abbreviation for Condensation Particle Counter,
906 SMPS is used for Scanning Mobility Particle Sizer. For more information the reader is referred to Andreae et al.
907 (2015).

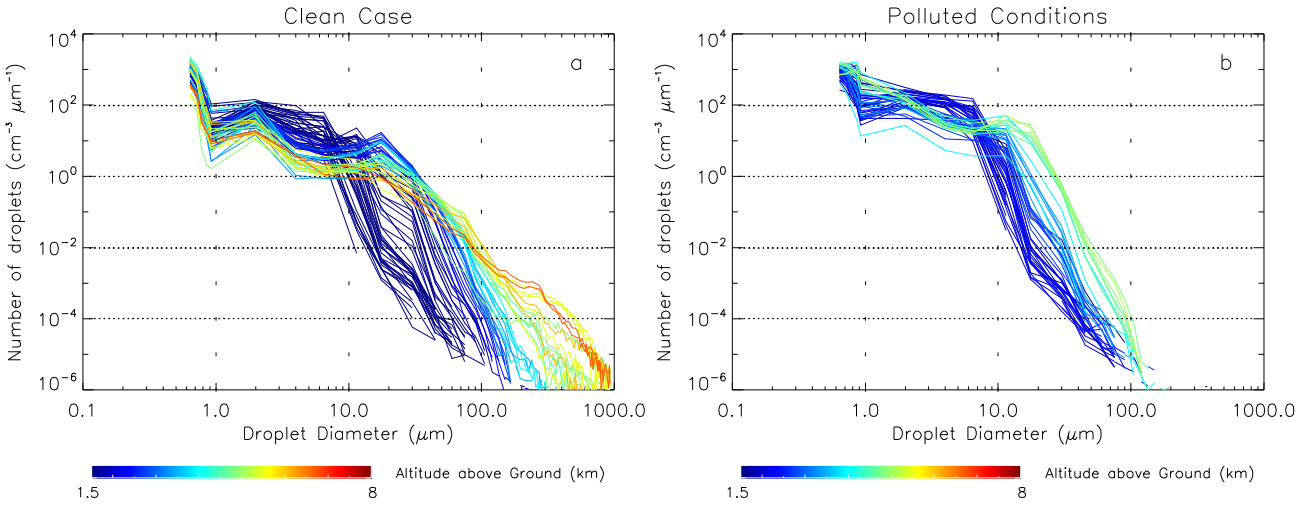

FIG. 9. Number size distributions of droplets in warm convective clouds measured with the NIXE–CAPS instrument. The colors of the lines indicate altitude above ground at which the measurements were taken. (a) flight AC09 (clean case), and (b) flight AC12 (polluted cloud influenced by biomass burning).

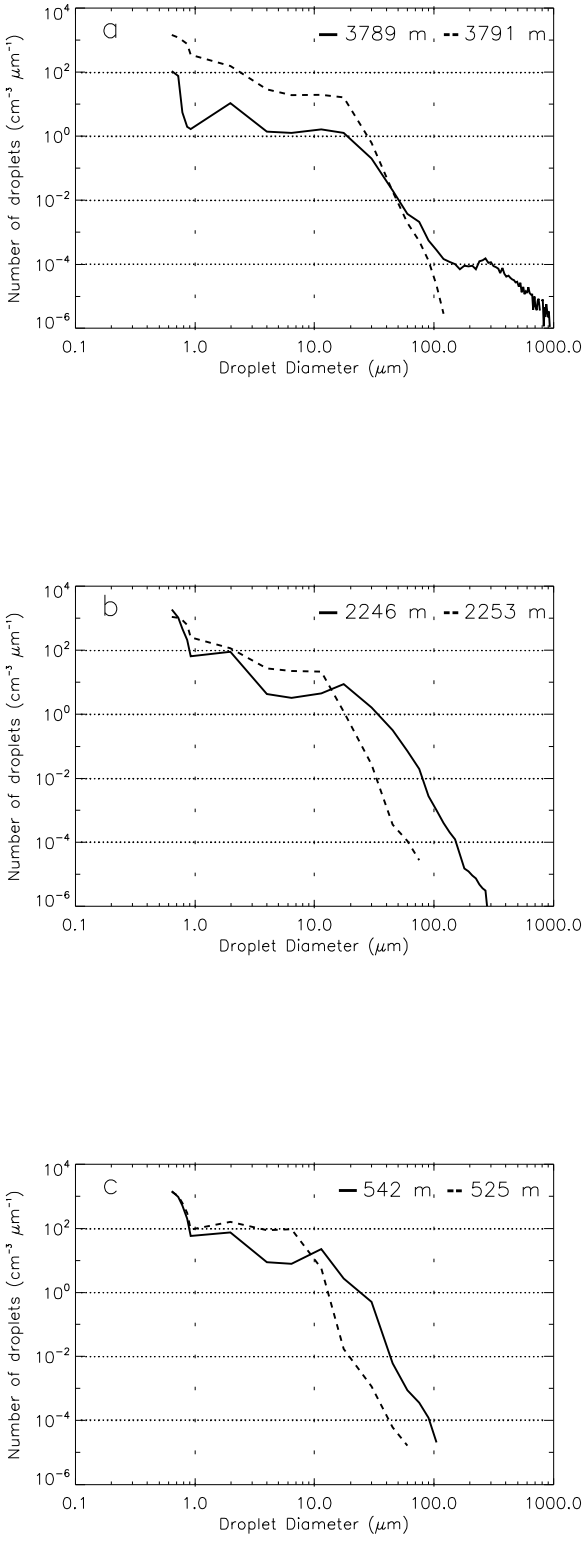

FIG. 10. Number size distribution of droplets in warm convective clouds measured with the NIXE–CAPS instrument during flight AC09 (clean case, solid line) and during flight AC12 (polluted conditions, dashed line) for different flight altitudes: (a) close to cloud top, (b) middle of cloud, and (c) near cloud base. The data were

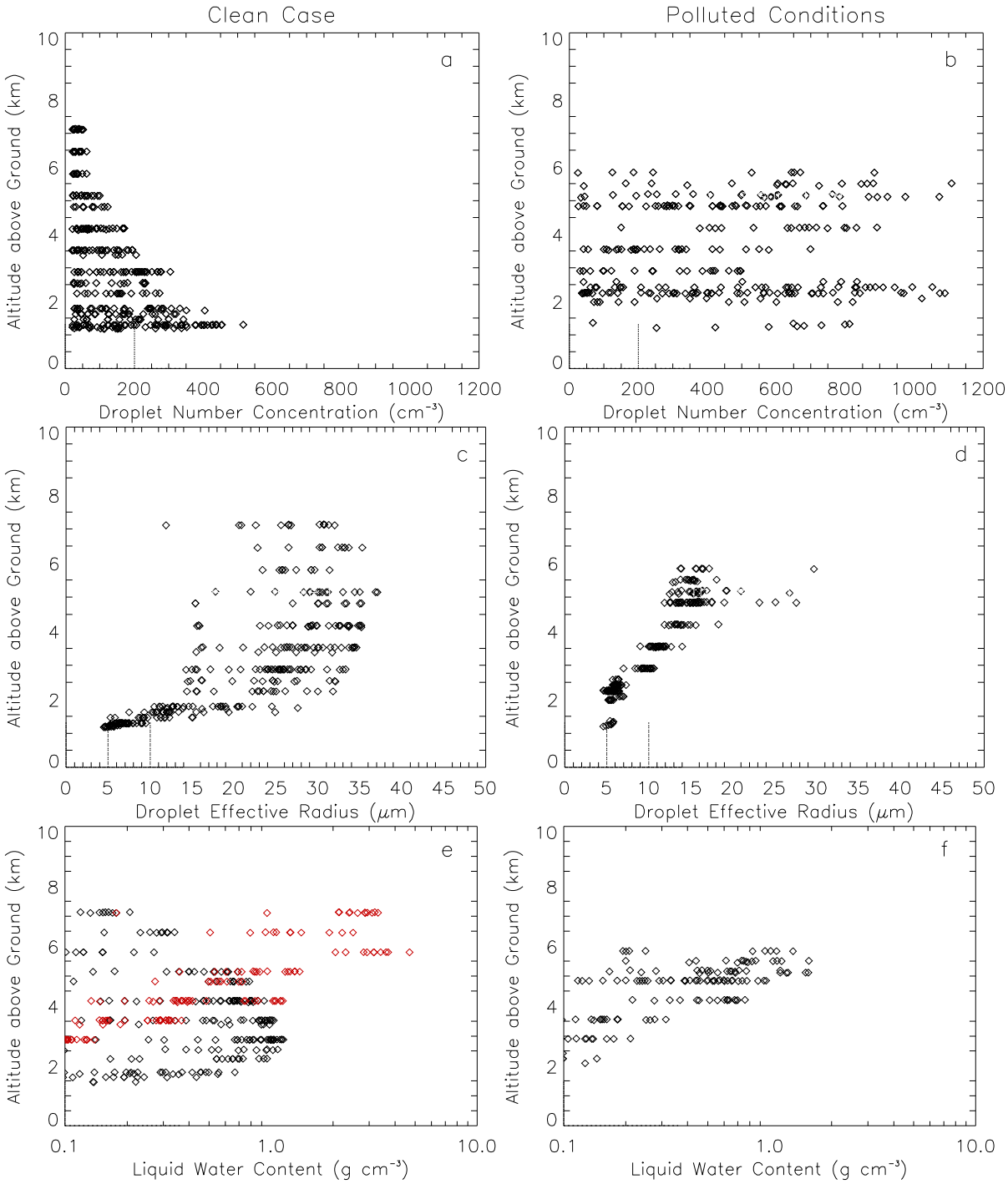

FIG. 11. Droplet number concentration (panels a and b), effective radius (c and d), and liquid water content (e and f) in warm convective clouds as a function of altitude calculated from the droplet size distributions shown in Fig. 9. The left panels (a, c, e) show the data from flight AC09 (clean case), and the right panels (b, d, f) from flight AC12 (polluted cloud influenced by biomass burning). In the lowest two panels (e and f) black symbols show the cloud LWC (considering particles with diameter smaller than 50 μm, measured by the CAS–DPOL), red symbols indicate rain LWC (including particles with diameter equal or larger than 50 μm, from CIPgs). The rain is suppressed in the polluted case (panel f).

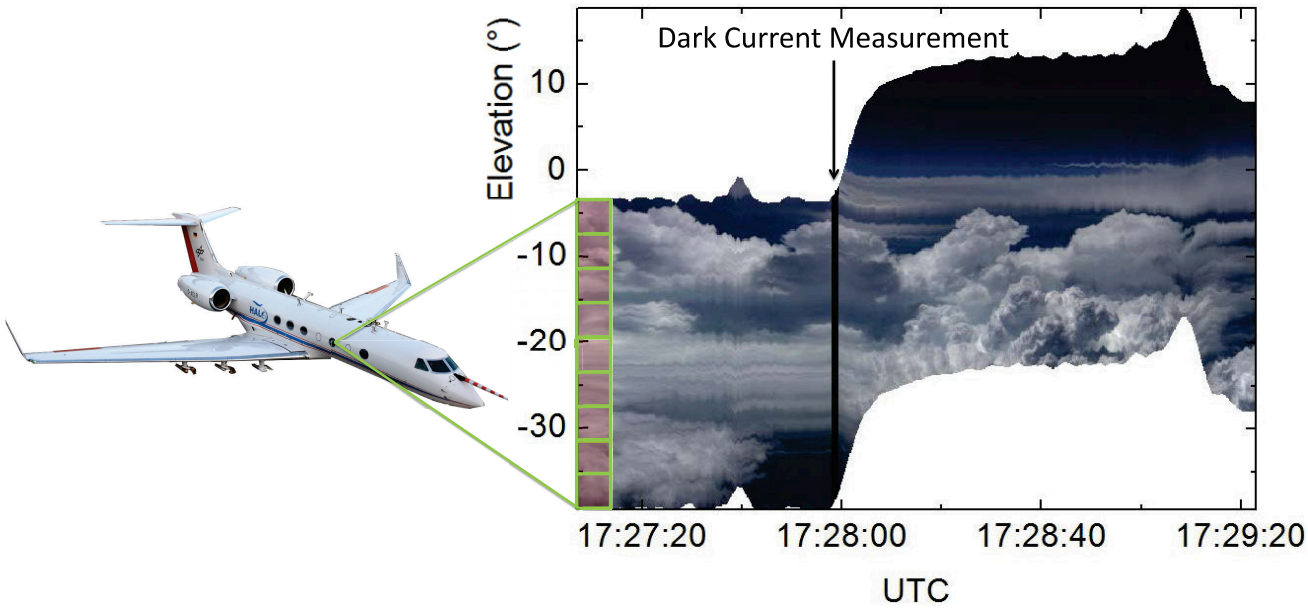

FIG. 12. Cloud–side observations of reflected solar radiances for a cloud during flight AC20. The black vertical line indicates a dark–current measurement. Changes of the elevation angle above/below horizon results from variable roll angles of the aircraft.

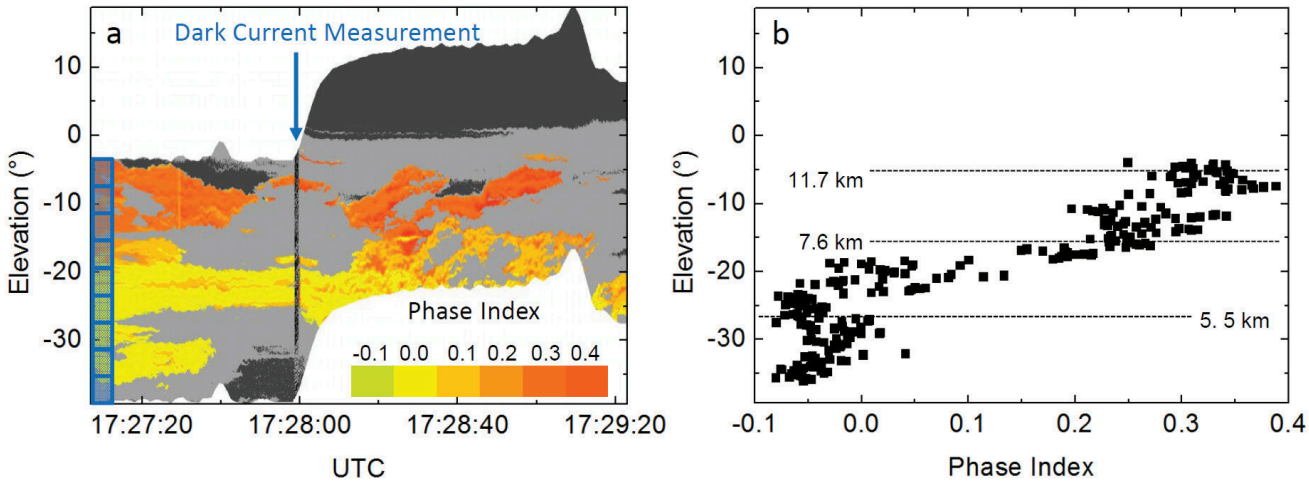

925 FIG. 13. Phase index derived from the specMACS measurements of cloud–side reflected radiances for the
926 same cloud as in Fig. 12 (from flight AC20). (a) Time series of vertical distribution of the phase index (side
927 view), recorded during a fly–by. The different colors represent values of the phase index. The dark grey areas
928 indicate cloudless portions or land surface; the light gray areas represent shadow zones of the cloud sides, which
929 are excluded from further analysis by an automatic cloud mask algorithm. These shadowed areas are not suitable
930 for phase index analysis. The black vertical line indicates a dark–current measurement. (b) Vertical profile of
931 phase index; three approximate altitudes (5.5; 7.6; 11.7 km) are allocated to vertical pixels.

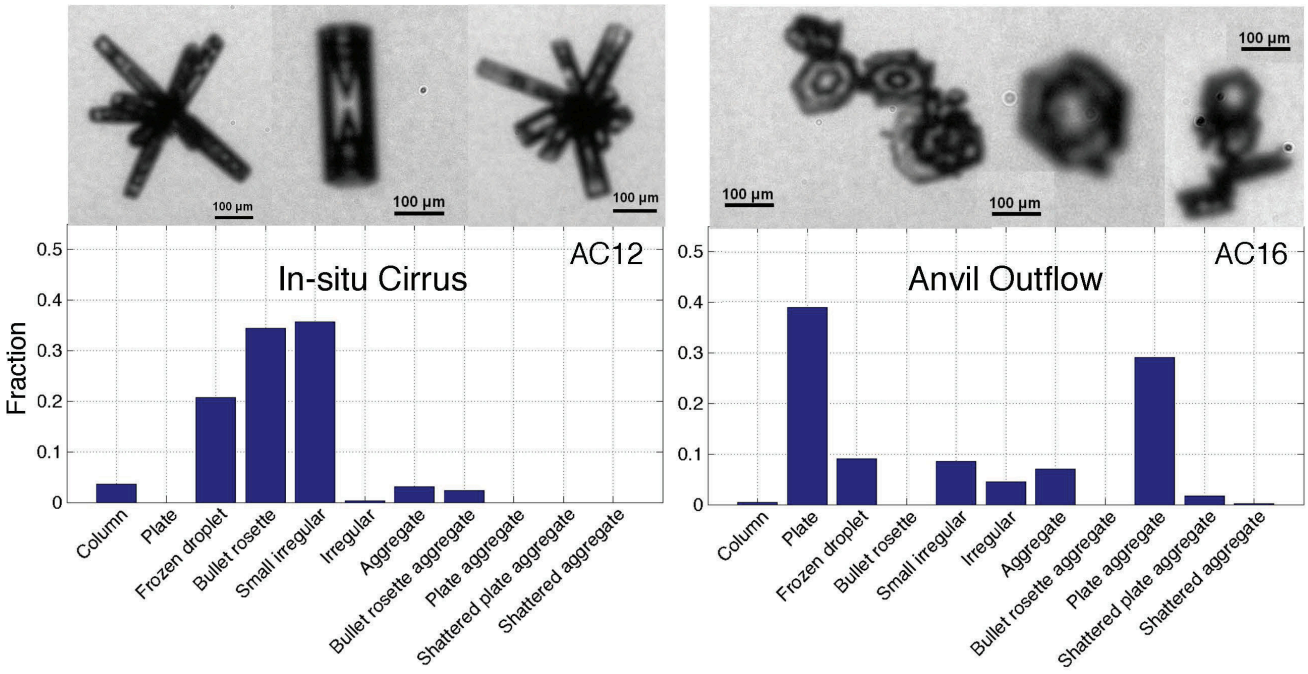

932 FIG. 14. Statistical analysis of the ice microphysical properties of ambient in–situ cirrus sampled during flight
933 AC12 and of an anvil outflow of a tropical convective system sampled during flight AC16. The analysis is based
934 on stereoscopic images taken by the PHIPS–HALO probe, which was newly developed for HALO.

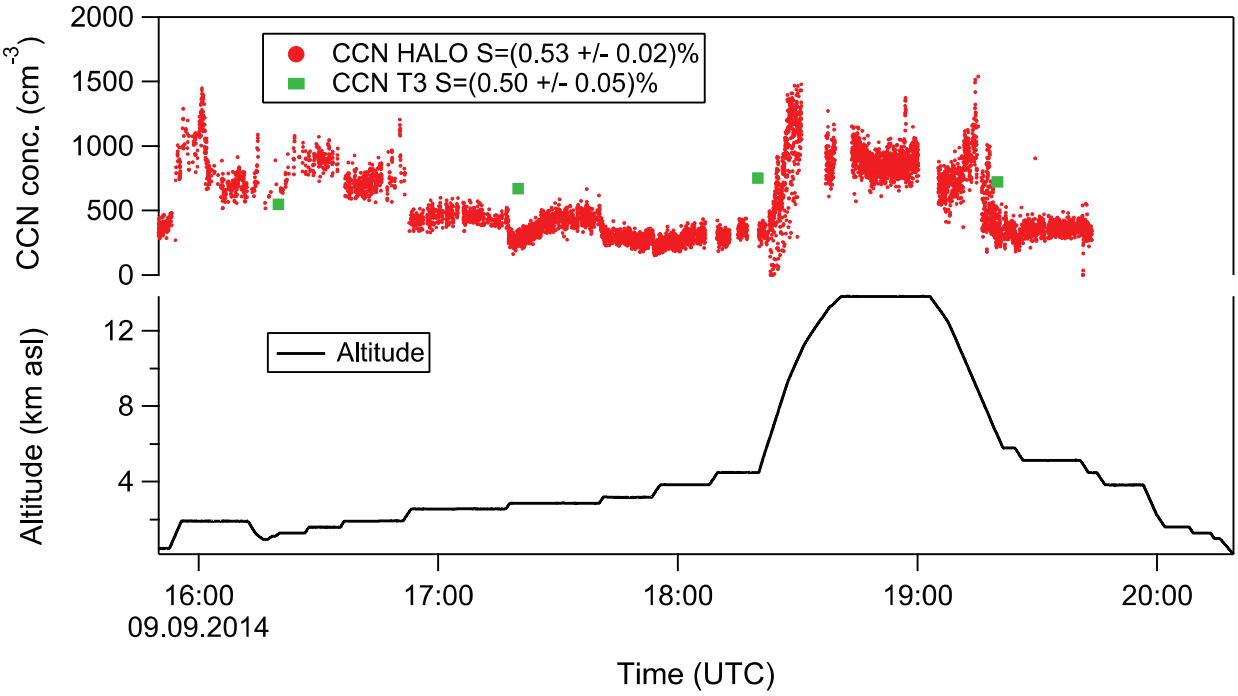

935 FIG. 15. Time series plot of CCN concentrations and altitude during flight AC08. The green markers represent
936 the CCN measurements performed at the T3 measurement site near Manacapuru. Particle number concentrations
937 have been normalized to standard air pressure (1000 hPa) and temperature (273.15 K).

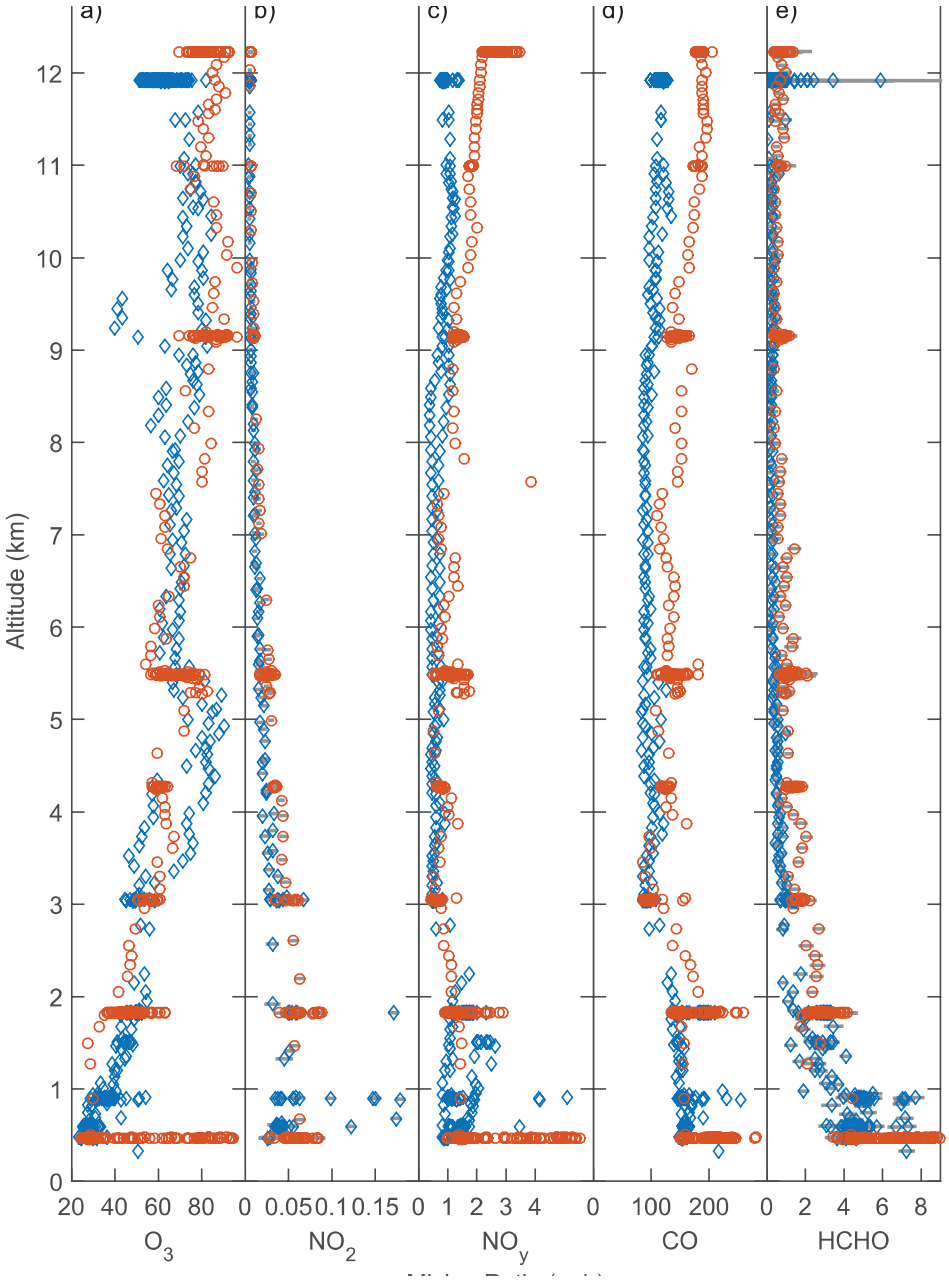

938 FIG. 16. Profiles of mixing ratios of O_3 (panel a), NO_2 (panel b), NO_y (panel c), CO (panel d), HCHO
939 (panel e) measured during flight AC11 on 16 September 2014. The southern leg of AC11 was performed
940 under notably more polluted conditions (open red circles) than the northern leg (open blue diamonds). The
941 cluster points indicate the variability of concentrations for individual altitudes measured at constant flight levels.
942 Unfortunately during flight AC11 the NO detection channel was not working.